McMASTER

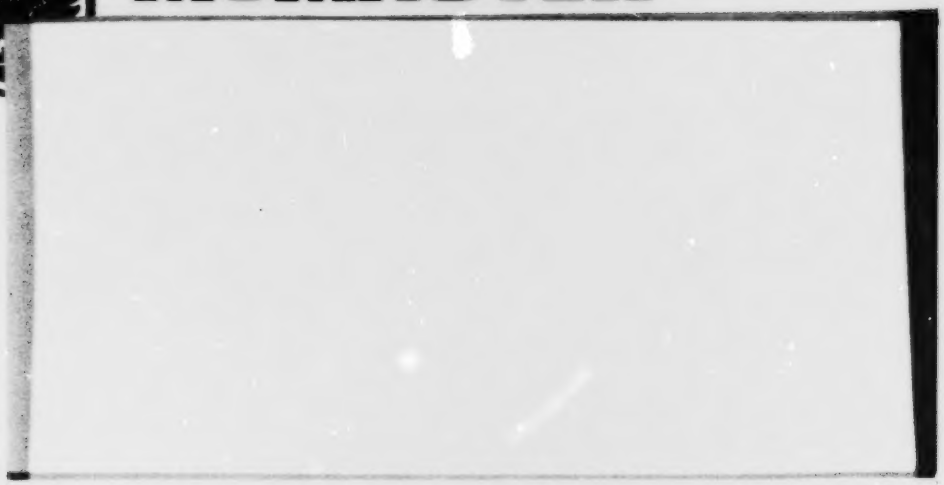

Engineering

86-1227/

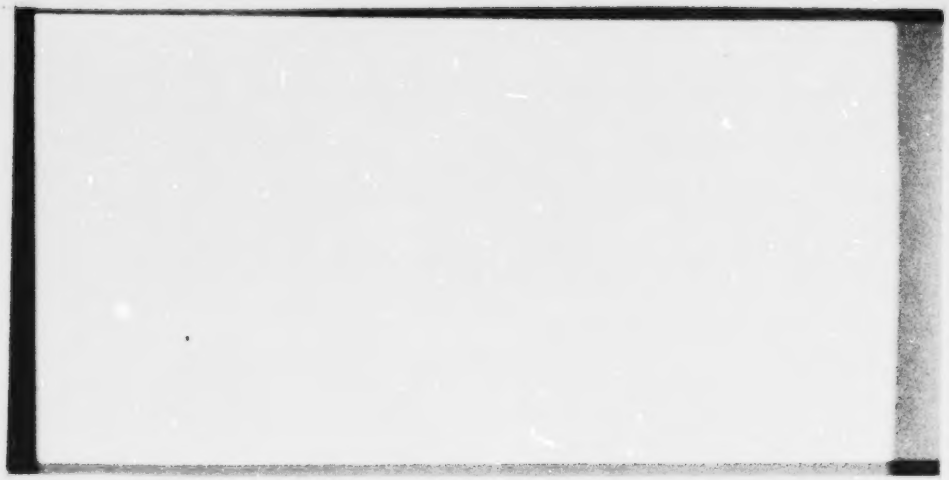

FACULTY OF ENGINEERING
McMaster University, Hamilton, Canada L8S 4L7
Telephone: (416) 525-9140 *Extension:* 4288 *Telex:* 061 8347

CONTRACT SERIAL NO. OSU81-00201

Final Report for the Project on

"MICROSTRUCTURAL FEATURES WHICH LIMIT FORMABILITY IN MASS PRODUCED COLD FORGINGS"

prepared for the

Department of Energy Mines and Resources - CANMET

under

DSS File No. 20SU.23440-0-9190

Scientific Authority:-

Dr. A.F. Crawley

Head, Metal Forming Section

Department of Energy Mines and Resources - CANMET

Principal Investigators:-

Dr. J.L. Duncan

Dr. J.D. Embury

Dr. R. Sowerby

Faculty of Engineering

McMaster University

59 pp

1. INTRODUCTION

This work has investigated mechanical test methods to determine the strain at fracture in samples of material designated for cold forging applications. An oft used test method has been the compression of a circular cylinder, Fig. 1(a), until the appearance of surface cracks. By altering the frictional conditions between the compression platens and the end faces of the cylinders, different amounts of barrelling can be promoted in the cylinders. In turn this controls the strain path at a point on the equatorial free surface of the specimen, and the amount of deformation that can be incurred before the onset of fracture. With ductile materials, even under very high interfacial frictional conditions, excessive deformation can ensue before the appearance of surface cracks. The associated deformation loads can be very large and there is always the danger of exhausting the capacity of laboratory testing machines. Another drawback with the cylindrical test pieces is the need to print or scribe a grid of lines on the surface to determine the strain at fracture. The grids are measured during the course of the test to reveal the hoop, ε_θ, and axial, ε_z, strain at a point on the equatorial free surface: the incompressibility assumption furnishes the radial, ε_r, strain.

In the present study two alternative upsetting tests have been proposed, and these have been named the collar test, Figs. 1(b) and (c), and the punch test, Fig. 1(d). Each of these tests results in lower fracture strains vis à vis the compression of circular cylinders, consequently they are to be preferred to promoting fracture in ductile materials. Furthermore with the collar test the surface grid can be dispensed with, the hoop and axial strains can be determined by measuring the diameter and thickness of the collar. The results obtained from the different upsetting tests indicate that the ε_θ and ε_z fracture strains do not lie on a single fracture line of slope $-\frac{1}{2}$, as proposed by Kuhn and his co-workers [1,2].

Once the ε_θ-ε_z strain path has been measured in any of the upsetting tests, the corresponding stress history can be revealed using simple plasticity theory. That is, the evolution of the hoop, σ_θ, and axial, σ_z, stresses can be determined during the course of the

test; the radial stress, σ_r, is of course zero at a point on the free surface. A knowledge of the stress and strain states permits the examination of several common fracture criteria. Damage functions proposed by Cockcroft and Latham [3] and Oyane [4] are investigated in this work.

Some details of the plasticity theory are given in the text, a fuller account is provided in Refs. [5,6]. It is necessary to introduce certain material characteristics into the plasticity (continuum) analysis. In the present study the material was classified by its representative stress ($\bar{\sigma}$) - representative strain ($\bar{\varepsilon}$) behaviour, as determined from either uniaxial tension or compression tests on the different materials. The stress-strain data were fitted using a simple power hardening law of the form

$$\bar{\sigma} = A\bar{\varepsilon}^n \text{ or } \bar{\sigma} = A(B+\bar{\varepsilon})^n .$$

The parameters A, B and n were evaluated using existing optimization routines [7] to obtain the best fit. Note that anisotropy was not considered in the continuum analysis, although it is recognised that if anisotropy is present this will influence the calculated values of the stresses [8].

It was found convenient to fit the experimentally determined ε_θ - ε_z data by a cubic spline function. This is not an essential feature of the analysis, although it did facilitate the evaluation of the corresponding stress state. Curve fitting using cubic splines was examined in some detail, although this was not central to the objectives of the research programme. A more comprehensive account of the curve fitting techniques can be found in Ref. [9].

The analysis of the upsetting tests, alluded to above, is dependent upon the experimentally determined ε_θ- ε_z strain path at a point on the free surface, and the application of simple plasticity theory to reveal the associated stress state. A more complex model of the upsetting tests was also attempted using a finite element (F.E.) technique. The material was assumed to be a rigid, incompressible, rate-insensitive solid, which obeyed the von-Mises yield criterion and associated flow rule. Mechanical property data were again determined from uniaxial tests, and the stress-strain behaviour was approximated by the power

hardening law: $\bar{\sigma} = A\bar{\varepsilon}^n$. The F.E. analysis permits the prediction of the stress and strain states at any point in the specimen throughout the deformation process. By adjusting the interfacial frictional conditions in the F.E. model, the predicted ε_θ - ε_z strain path at a point on the equatorial free surface of the test specimens could be made to correlate quite well with the experimental results. However, the F.E. model does not predict the onset of fracture, this could only be achieved by establishing some reliable failure criterion. Some of the F.E. results are discussed in the body of the text, and some typical input and output are given in an appendix to this report. Further details of the analysis are provided in Refs. [10-12]. A listing of the program in FORTRAN is available.

In the present work the flow and fracture characteristics of three medium carbon steels, a eutectoid steel and an Fe-1.2P alloy were studied in various upsetting tests. The materials were subjected to different heat treatments, consequently a number of different structures were available for investigation. A comprehensive account of the fracture studies is given in Ref. [13].

The subsequent sections of this report describe the salient features of the work conducted in the research progamme. The report would be too voluminous if each aspect of the programme was given in extenso. For this reason a number of McMaster reports, articles, etc., compiled during the course of the work, should be consulted. One copy of each of these documents will be sent to Dr. A.F. Crawley. The documents are:

a) A Master of Engineering thesis by O'Reilly [13], dealing with the materials, their preparation, testing, quantative metallography and fracture studies.

b) A report on the F.E. analysis prepared by Dr. N.L. Dung [12]

c) An account of the upsetting tests using simple plasticity theory [5,6].

d) Curve fitting by cubic splines [9].

The reference numbers relate to the Bibliography at the end of this report.

2. EXPERIMENTAL PROCEDURE

2.1 General Remarks

The upsetting tests considered in this study have already been alluded to, and the geometry of the test pieces is shown in Fig. 1. End flanges are provided on the collar sample of Fig. 1(c). These fit into recesses in matching platens, and it was considered this provided better alignment of the end faces during the test.

Prior to the commencement of this work, Brownrigg et al. [14] had conducted a series of upsetting tests on a variety of commercial steels in a hot-rolled condition. All the materials possessed a ferrite-pearlite microstructure. Three test piece geometries were employed corresponding to Figs. 1(a), (b) and (d), although the dimensions of some of Brownrigg's samples varied slightly from the nominal sizes quoted in Fig. 1.

Some results taken from Ref. [14] are shown in Fig. 2 for an AISI 1045 steel. The hoop, ε_θ, and axial, ε_z, strains were determined from measurements of a 1.27 mm square grid for the specimens shown in Figs. 1(a) and (d), and directly from the collar for the sample of Fig. 1(b). The influence of the specimen geometry on the shape and level of the ε_θ-ε_z strain path is apparent from Fig. 2. Note the essentially linear strain path for the collar test, with a slope $\varepsilon_\theta/\varepsilon_z \simeq -2$. The behaviour illustrated in Fig. 2 is quite typical of all the materials tested in Ref. [14], and results from the present study corroborate the general nature of the ε_θ- ε_z strain paths.

It would appear from Fig. 2 that no single fracture line, as proposed in [1], adequately fits all the data. The line with a slope $\varepsilon_\theta/\varepsilon_z = -\frac{1}{2}$ and which intersects the ordinate at $\varepsilon_\theta \simeq 0.3$ is an estimate of a fracture line for the tests performed on the circular cylinders only i.e. the test procedure of Fig. 1(a). Different strain paths for this test can be generated by altering the interfacial frictional conditions and/or the height to diameter ratio of the cylinders.

2.2 The Present Study

This section of the report summarises some of the test procedures carried out by O'Reilly and discussed at length in a recent Master of Engineering, thesis [13].

2.2.1 Materials

As stated previously the materials used in the present study were A.I.S.I. grades 1045, 1144, 1541 and 1095 steels. The 1045 and 1095 are regular plain carbon grades whereas 1144 and 1541 contain additional amounts of sulfur and manganese respectively. Samples of a Fe-1.2P alloy prepared by U.S. Steel were also tested. Table 1 shows analyses of all the materials in weight percentages.

2.2.2 Sample Preparation and Heat Treatment

All of the materials were obtained in the form of cylindrical rods. In the case of 1045, 1144 and 1541 the rods had been cold drawn, the 1095 was in the as hot rolled condition and the Fe-1.2P had been cold swaged to rod form. In all cases the test samples were first machined and then heat treated after machining in order to facilitate the development of the shear failure mode [15].

True stress-true strain curves in tension were obtained for all the materials and in compression for 1045 and 1144. After machining, groups of 1045, 1144 and 1541 samples were heat treated in the following manner:

Annealing:

1) Samples were sealed in a small steel box packed with coke chips,

2) annealed in a muffle furnace at 850°C $\pm$ 3°C for 2 hours,

3) furnace cooled.

Spheroidizing:

1) Samples were sealed in a small steel box packed with coke chips,

2) annealed in a muffle furnace at 710°C $\pm$ 3°C for 24 hours,

3) air cooled.

Decarburizing:

1) Samples were individually suspended in a verticle tube furnace,

2) furnace purged with Ar and heated to 850°C,

3) the gas mixture switched to wet H_2, maintained for 2 hours,

4) samples furnace cooled in Ar.

The purpose of the coke chips in the annealing and spheroidizing treatments was to prevent surface decarburization of the samples. Later metallographic observations showed that this procedure was effective. The spheroidizing cycle employed was chosen because it closely follows common industrial practice for cold heading grades.

The Fe-1.2P was heat treated in order to obtain an intergranular mechanism of failure, the heat treatment was:

1) Samples were placed in a quartz tube under high vacuum,

2) soaked at 850°C $\pm$ 3°C for 24 hours,

3) water quenched.

2.2.3 Uniaxial Testing

Tensile samples, 5 mm in diameter and 25 mm gauge length, were pulled to fracture in an Instron machine at a cross-head speed of 0.5 mm/min. Since the cross-head speed was constant the strain rate varied throughout the test. Initially it was approximately 3.5×10^{-4}/s and increased by a factor of 10 once necking commenced. The neck shape was monitored and the Bridgman correction factor [16] was employed to calculate the $\sigma - \varepsilon$ relationship.

Cylindrical compression tests were also performed on the materials at a comparable deformation rate to the tensile tests. Smooth compression platens were employed and the tests were interrupted to renew the teflon tape which served as a lubricant. The deformation was close to homogeneous. The calculated stress- strain relationships agreed very well with those determined from the tensile tests.

The mechanical property data is summarised in Table 2, the stress-strain relationship has been approximated by the power hardening law: $\bar{\sigma} = A\bar{\varepsilon}^n$.

2.2.4 Upsetting Tests

The majority of the upsetting tests were performed on the specimens shown in Figs. 1(a) - 1(c). Unfortunately time did not permit a detailed study of the punch test of Fig. 1(d), with all the materials. Some preliminary tests with the 1045 material confirmed the findings of Brownrigg et al. [14].

Some typical data for the 1045 steel in the compression test i.e. the test method of Fig. 1(a), is provided in Fig. 3. Note it was not possible to fracture the spheroidized and decarburized samples. The fracture data obtained for all the materials in the compression test are summarized in Table 3. A minimum of two samples were compressed for each test. The calculated stresses at fracture, determined from the strain path data, are illustrated in Table 6. These latter figures should be taken merely as an indicator of the stress levels involved. The calculated stresses, using the simple plasticity theory, depend very heavily on an accurate determination of the slope of the ε_θ-ε_z curve, which is prone to experimental error particularly close to the point of fracture. Carrying out repeated tests would improve the confidence that could be placed on the calculated stress values. Also shown in Table 6 are the Cockcroft integrals based on the stress and strain states, and the estimated instability strains based on an analysis due to Thomasen [20] and originally evaluated in [13].

Collar samples corresponding to Figs. 1(b) and (c) were prepared from all of the materials. The test piece geometry appeared to have little influence on the results. For the 1045 and 1144 steels a large number of samples were deformed to fracture in order to obtain an estimate of the range of failure strains that could be obtained for each material and heat treatment. For 1045, ten samples in each heat treated condition were tested, and for 1144 twenty samples were tested.

It was observed that with all the materials the experimentally determined strain paths were essentially linear. However, there was a variation in the slope with the individual tests. This was from a slope $\varepsilon_\theta/\varepsilon_z \simeq -2$ towards plane strain, the average slope was approximately -3.

The fracture data are shown in Table 4, and because of the large number of samples tested for the 1045 and 1144 steels, some statistical analyses were performed on the data. Table 4 lists the standard deviation of the fracture strains.

Table 7 lists the calculated stress states at fracture as determined from the strain path data. Also quoted in the table is the calculated Cockcroft integral and the predicted instability strain.

2.2.5 Metallographic Preparation and Observation

The samples from the various tests were sectioned in the longitudinal and transverse directions. In the case of the tensile and collar tests sections of the actual fracture surface were also mounted for examination in the S.E.M.. The polishing procedure used is standard and is listed below.

1) Samples were mounted in lucite
2) Surface ground on Silicon-Carbide papers, 240, 320, 400 and 600 grit
3) Polished on 6 μm diamond wheel
4) Polished on 1 μm diamond wheel
5) Etched in Nital (2%) for 10 sec.

After the samples were polished and etched they were mounted on stubs for the S.E.M. using silver electrodag. A Philips 301 S.E.M. was employed for the observations using an accelerating voltage of 15 KV and a 500Å spot size.

A quantitative metallographic examination of the inclusion characteristics of four of the steels was made using a Leco model 720 instrument. The analysis was made at 700x based on 50 fields of observation. Observations of the bulk, center, and surface regions were

made, and the results are shown in Table 5(a). A quantitative analysis of the MnS inclusion size distribution in the 1144 steel is shown in Table 5(b).

3. THEORETICAL CONSIDERATIONS

3.1 Simple Plasticity Theory

The following illustrates the theoretical fundamentals to arrive at the stress state assuming the ε_θ-ε_z strain path is linear.

3.1.1 Linear Strain Path

For a linear strain path, it follows that

$$d\varepsilon_\theta/d\varepsilon_z = \varepsilon_\theta/\varepsilon_z = \alpha. \tag{1}$$

The representative strain is

$$\bar{\varepsilon} = 2/\sqrt{3}\,(1 + \alpha + \alpha^2)^{1/2}\,\varepsilon_z\,. \tag{2}$$

Since the radial stress, σ_r, is zero at the free surface, then if the material is assumed to obey the von Mises yield criterion and associated flow rule, it follows that

$$\sigma_\theta = (1 + 2\alpha)/(2 + \alpha)\,\sigma_z\,, \tag{3}$$

the representative stress is

$$\bar{\sigma} = 1/(2 + \alpha)\,\{3(1 + \alpha + \alpha^2)\}^{1/2}\sigma_z\,, \tag{4}$$

and the hydrostatic stress

$$\sigma_m = 1/3\,(\sigma_\theta + \sigma_z)\,. \tag{5}$$

The representative stress-strain data for the steels was expressed as a simple power hardening law [17]

$$\bar{\sigma} = A\bar{\varepsilon}^n\,, \tag{6}$$

the coefficients A and n having been determined from uniaxial compression tests. Therefore, given (6) and the slope α, the stress history can be determined from equations (1) to (5). Anisotropy has not been accounted for, but if it is considered, the selected model should reflect

the state of the material. There seems little point in adopting a simple anisotropic model, such as the one proposed by Hill [18], if this does not correspond to the material behaviour.

Cockcroft and Latham [3] proposed that fracture would occur when

$$\int_0^{\bar{\varepsilon}_f} \sigma^* \, d\bar{\varepsilon} = C, \tag{7}$$

reaches a critical value, say C. The quantity σ^* is the peak tensile stress in the process and in the upset tests would normally correspond to the hoop stress σ_θ, the representative fracture strain is denoted by $\bar{\varepsilon}_f$. Oyane [4] considered a void growth model and postulated that

$$\int_0^{\bar{\varepsilon}_f} (1 + \frac{1}{C_1} \frac{\sigma_m}{\bar{\sigma}}) \, d\bar{\varepsilon} = C_2. \tag{8}$$

Note the material constants C, C_1 and C_2 in (7) and (8) have to be determined from experiment, and it will require two distinct tests to evaluate the constants for the Oyane integral.

An explicit expression can be obtained for C, i.e.,

$$C = \frac{(1 + 2a)}{[3\,(1 + a + a^2)]^{1/2}} \frac{A}{(n+1)} \bar{\varepsilon}_f^{(n+1)}, \tag{9}$$

and by the use of (2), the representative fracture strain can be replaced by the axial strain at fracture. Similarly, an explicit expression can be obtained for the hydrostatic stress term in the Oyane integral, i.e.

$$\int_0^{\bar{\varepsilon}_f} \frac{\sigma_m}{\bar{\sigma}} \, d\bar{\varepsilon}.$$

If we define the integral as H, then

$$H = \frac{1 + a}{[3\,(1 + a + a^2)]^{1/2}} \bar{\varepsilon}_f, \tag{10}$$

and the Oyane integral becomes

$$\bar{\varepsilon}_f + \frac{H}{C_1} = C_2 \tag{11}$$

3.1.2 Non-linear Strain Paths

A similar procedure to the foregoing follows if the path is non-linear. In this case it was found to be an expedient to express ε_θ as an analytical function of ε_z, and for this purpose a cubic spline function approach was adopted using three knot (or joint) positions. The spline functions are fitted to each interval between the knots, with continuity of the first and second derivatives of the functions ensured at each interior knot position. The underlying theory is to be found in Ref. [19], while the application of the method to fitting the representative stress-strain curve of sheet steels is given in Ref. [9].

From the cubic spline interpolating function to the ε_θ-ε_z data, the first derivative gives the slope α at any desired value of ε_z. The full range of ε_z was divided into an even number of intervals, each interval covering approximately 2% strain. The first derivative α was assumed to be constant in each interval, and it was found that the strain interval was small enough to avoid any unacceptably large discontinuities in the calculated stress components, vide [5] The representative strain, $\bar{\varepsilon}$, was accumulated for each successive interval of $d\varepsilon_z$ by repeated application of (2). The corresponding representative stress is evaluated from (6) and the stress components from equations (3) to (5).

Figure 4 shows the variation of σ_z, σ_θ and σ_m with $\bar{\varepsilon}$ as determined from the compression of a circular cylinder of AISI 1045 steel, the results refer to specimen B1 in Figure 2. The variation of the stress components is typical of the compression test, i.e. the test method of Fig. 1(a). The degree of barrelling of the cylinder controls the rate at which the hydrostatic stress changes from compression to tension. Note that the behaviour of the hydrostatic stress component in the compression test is quite different from that which arises

in the collar test. With the collar test the ε_θ-ε_z strain path is essentially linear, with a slope, $\varepsilon_\theta/\varepsilon_z$, in the vicinity of -2. In this case, the hydrostatic stress is tensile from the outset, and this is likely to be a factor in producing lower fracture strains in the collar test.

3.2 Finite Element Analysis

In the present work the material is assumed to be an incompressible, rate- insensitive, rigid plastic solid, which obeys the von Mises yield criterion and associated flow rule. The finite element method employed is based on Markov's principle, but with certain modifications embodied into the variational principle. The incompressibility condition is introduced by means of a Lagrange multiplier, and the influence of friction at the interface between the workpiece and dies is accounted for by regarding the friction work as internal energy dissipation in the variational principle. The use of linear elements was found to be satisfactory, and this gives rise to constant stress and strain components within each element. The technical details of the adopted finite element scheme are to be found in Refs. [10- 12].

In closed die and many open die forging operations, as the deformation proceeds the free surface area of the workpiece is reduced as more material makes contact with the dies. Thus in the analysis it is necessary to continuously modify the contacting surface and to check that the ensuing frictional stress and velocity at a contacting boundary node are physically compatible. In the present analysis the frictional stress at the interface was represented as

$$\tau = mk \qquad (12)$$

where $0 \leq m \leq 1$ and k is the shear stress of the material. For the compression test shown in Figure 1(a) the following conditions were considered;

i) $0 \leq m \leq 0.25$, to represent a well lubricated condition.

ii) $m = 1.0$ to represent an unlubricated condition with material shearing across the platens.

iii) sticking friction, such that there is no relative sliding once the material comes into contact with the platens.

For the punch tests of Fig. 1(d), m was selected as either 0, 0.1, 0.25 or 1.0. For each of the collar tests in Figs. 1(b) and (c), a sticking friction condition was assumed. With the geometry shown in Fig. 1(b), material from the cylinder wall is folded back to contact and adhere to the platens as the test progresses. No lateral flow of the end flanges is possible with the test piece shown in Fig. 1(c), since they locate in recesses in the compression platens. In this case, the cylindrical portion of the test piece between the end flanges and central collar are bulged out. At higher reductions, the bulging can be so severe that contact is made with the end flanges and the central collar. Overlapping of the F.E. mesh can ensue and the numerical solution is terminated at this stage.

Due to the symmetry of the specimens shown in Fig. 1, only one-quarter of the test piece needs to be considered in the analysis. Up to 100 quadrilateral elements were used in the F.E. mesh to characterize each specimen.

The stress-strain behaviour of the material was approximated by the power hardening law

$$\bar{\sigma} = A(B + \bar{\varepsilon})^n ,$$

which can also provide a measure of the initial yield stress, Y_0, of the material where

$$Y_0 = AB^n .$$

Some results from the F.E. analysis are presented later in this report. A more complete account of the analysis and the numerical results is provided in Ref. [12]. A complete program listing, in the FORTRAN language, for an upsetting test is given in Appendix A.

4. RESULTS AND DISCUSSION

4.1 Finite Element Analysis

4.1.1 Strain Path Calculations

Figure 5 shows the comparison between the predicted and experimentally determined ε_θ-ε_z strain path for the compression test of Fig. 1(a). The material was an AISI 1045 steel in either a spheroidized (S) or annealed (A) condition. The strains were evaluated

at a point on the equatorial free surface. The results are quite typical, and by altering the interfacial frictional condition in the F.E. model, excellent agreement can be obtained.

Some results for the punch test, see Fig. 1(d), are given in Fig. 6 for an annealed 1045 steel. Predicted and experimental data for the collar test of Fig. 1(b) is illustrated in Fig. 7. Again, the material is a 1045 steel in either an annealed or spheroidized condition. The strain path is calculated for two locations in the collar specimen. The location F is a point on the free surface of the collar, while the location E is an interior point - see the inset diagram in Fig. 7.

4.1.2 Stress Calculations

Figure 8 shows the calculated hoop, σ_θ, axial, σ_z, radial, σ_r, and hydrostatic stress, σ_m, at a point on the equatorial free surface during the compression test. The calculations have been performed for an annealed 1045 steel, assuming sliding friction with $m = 1.0$. In practice, σ_r should be zero at the free surface. The small negative value of this stress component in the F.E. analysis arises because an average value is calculated within an element, and only one side of the element is contiguous with the free surface. The small oscillations in some of the stress components at larger reductions is another feature of the F.E. calculations. The analysis allows for one complete element only (and not part of an element) being folded from the side of the cylinder to come into contact with the platens. Hence, there is an abrupt change in the contact area. These undesirable features can be minimized by reducing the size of the mesh.

Similar calculations for the collar test of Fig. 1(b) are shown in Fig. 9; again, for an annealed 1045 steel. The calculations have been performed for two locations within the specimen referred to earlier, i.e. point E shown in Fig. 9(a) and point F in Fig. 9(b).

Note that for all the upsetting tests, the theory predicts that the hydrostatic stress at the free surface becomes progressively more tensile as the deformation proceeds. For the collar tests, the hydrostatic stress is tensile from the outset, while for the compression and

punch tests, it is initially compressive and the rate of change to a tensile state increases with increasing interfacial friction.

4.1.3 Material Flow Patterns

The F.E. analysis permits the determination of the velocity or displacement vectors of each nodal point within the mesh during the course of an upsetting operation. In the present work, the hardening behaviour of the material had little influence on the gross flow characteristics in any given test. Figure 10 illustrates the results that can be obtained from the computer program. The diagram pertains to the collar test of Fig. 1(c) for a spheroidized 1144 steel.

At present no predictive failure criterion has been found which can be incorporated into the F.E. model. However, the analysis does reveal the stress and strain state at every point in a test piece throughout the deformation. Hence all the principal macroscopic quantities are known for future adoption in a failure criterion. It should be noted that the computational costs are small. It takes about 8 minutes on a CDC 6400 computer to arrive at the stress and strain states and the flow patterns for a complete upsetting test.

4.2 Simple Plasticity Theory

The technique for calculating the stress state for both linear and non-linear strain paths has already been referred to. Figure 4 shows some typical results for the variation in the stress components, as a function of $\bar{\varepsilon}$, during the compression of a 1045 cylinder.

The Cockcroft and Oyane integrals for this same material deformed in three different upsetting tests, refer to Fig. 2, are listed in Table 8. It is clear that the integrals are not constants for all the upsetting tests. Also shown in the table is the integral of the hydrostatic stress, i.e.

$$\int_0^{\bar{\varepsilon}_f} \sigma_m \, d\bar{\varepsilon} \, ,$$

and again no obvious pattern emerges. However, to a first approximation the hoop stress, σ_θ, at fracture is constant, and this suggests that a possible fracture criterion for the material is the maximum shear stress hypothesis.

As already remarked the fracture strains for the upsetting tests shown in Fig. 2 did not lie on a single fracture line of slope $-\frac{1}{2}$. However, let it be assumed that such a fracture locus does exist and its equation is given by

$$\varepsilon_\theta = \varepsilon_\theta^* - \frac{\varepsilon_z}{2} , \tag{13}$$

where ε_θ^* is the intercept value when $\varepsilon_z = 0$. For linear straining paths, $\varepsilon_\theta/\varepsilon_z = \alpha$ and therefore the axial strain at fracture is determined from (13) as

$$(\varepsilon_z)_f = \varepsilon_\theta^*/(\alpha + 1/2) . \tag{14}$$

The integrals in (7) and (8) were evaluated assuming linear straining paths (α = constant) and that $\varepsilon_\theta^* = 0.3$. The latter value was taken from Fig. 2 which is an estimate of the fracture line intercept for the compression tests only. The material characteristics were also chosen to correspond to the 1045 material quoted in Fig. 2. The calculations are shown in Table 9. As can be seen the Cockcroft integral is essentially constant in the region close to plane strain. It increases slightly in the domain $-10 \leq \alpha \leq -1$, followed by a much more rapid increase as homogeneous compression, $\alpha = -1/2$, is approached. The Oyane integal shows very similar characteristics within the range $-10 \leq \alpha \leq -1/2$, but in contrast it begins to rise again as the plane strain condition is approached. The coefficient C_1 in the Oyane integral was selected as 0.48, the figure was the average of a number of initial trial strain paths. Also given in Table 9 is a hydrostatic stress integral,

$$\int_0^{\bar{\varepsilon}_f} \sigma_m \, d\bar{\varepsilon} .$$

This is not a constant, it is zero when $\alpha = -1$, increases rapidly in the domain towards homogeneous compression but gets increasingly more negative towards plane strain.

If a single fracture line exists then it transpires that there is little difference in the Cockcroft and Oyane integrals if the fracture line is reached along a curved or linear strain path. This fact was discovered after many different calculations. However evidence can also be found by comparing the Cockcroft and Oyane integrals in Table 8, for the compression tests only, with those given in Table 9.

4.3 Fracture Studies

This section summarizes the discussion provided in Ref. [13], which should be consulted for further details.

4.3.1 The Role of Test Piece Geometry

The lower fracture strains attained in the collar test vis à vis the compression test is clearly a feature of the specimen geometry; this governs the deformation mode and the associated stress state. It is well documented that the presence of a hydrostatic stress acts to suppress both the nucleation and growth of microstructural damage. Thus it would appear that the success of the collar test in promoting fracture in ductile materials is due to the higher level of tensile triaxility induced in the test piece.

With sufficient lubrication in the compression test homogeneous deformation can be achieved. In this case only one principal stress exists and this is compressive in nature. Thus any fracture criteria based on the existence of tensile stresses is inappropriate in these cases. As is well known from compression tests on ductile materials, fracture can be delayed almost indefinitely in the homogeneous mode.

It has been proposed by Kudo and Aoi [21], as well as other workers, that during upsetting tests cracking can initiate and propogate along planes bearing the highest shear

stress. Since σ_r is always zero at the free surface, the maximum shear stress will lie either in the z-θ or r-z plane depending upon the magnitude and sign of σ_z in comparison to σ_θ.

It was found that when compressing cylinders of 1095 steel that fracture occurred at 45° to the z-θ plane, see Fig. 11. Hence it concluded that if the fracture is shear induced, then σ_z and σ_θ control the shear. In all the tests with the medium carbon steels, including the collar test, it was generally observed that cracks propogated at 45° in the r-θ plane. The cracks appeared as longitudinal splits on the surface of the test piece, i.e. the z-θ plane.

In materials which displayed a higher ductility, i.e. the 1045 and 1541 steels, a surface instability was sometimes observed in the collar test, see Fig. 12. In some, but not all cases, the voiding within the interior of the collar appears to have nucleated around the presence of readily identifiable large (or aggregates of) inclusions.

4.3.2 Fracture Mechanisms in Compression

In this study three types of fracture behaviour have been observed; ductile fracture, ductile failure terminated by macroscopic shear, and intergranular fracture. In the medium carbon steels ductile fracture was the only fracture mechanism observed. This mechanism is commonly characterized by three stages; the nucleation, growth, and coalescence of voids. In commercial materials voids generally nucleate by either decohesion at the particle-matrix interface or by fracture of the particles. The strain to failure can be expressed as the sum of the strains obtained during each stage of the process;

$$\varepsilon_f = \varepsilon_N + \varepsilon_G + \varepsilon_C$$

Since the damage tends to condense to very localized volumes, the contribution of the coalescence strain is small and generally ignored. The nucleation strain is expressed as a discrete value in the above expression, however, it has been observed [22] that this strain is a function of numerous microstructural characteristics. Among these are, interface and particle strength, particle size and volume fraction, and the orientation and shape of the

particles. This indicates that void nucleation probably occurs over a range of strains beginning at large inclusions or groups of inclusions where the local stresses are highest.

The most commonly used models of void growth are those of Rice and Tracey [23] and McClintock [24]. The Rice and Tracey model describes the growth of an isolated void while the model of McClintock is restricted to a regular array of voids. Brown and Embury [25] have suggested a coalescence criterion based on the void growing until its size is equal to the average interparticle spacing. When this size is reached the fracture process is terminated by localized shear between neighbouring voids. Generally, predictions of fracture based on the above models tend to over estimate the fracture strain.

The results of the collar tests, Tables 4 and 7, confirm that increasing inclusion content leads to a rapid decrease in ductility. The effect of the MnS inclusions is expected to be two-fold, because of their low interface strength they nucleate cavities at very low strains, and secondly, they also limit the extent to which growth must occur before fracture takes place. A comparison of the fracture strains in tension with those observed in the collar tests shows markedly lower strains in the collar tests. Although the stress states in the two tests are similar the maximum tensile stress in the collar test is at right angles to the inclusion stringers whereas in the tensile test it is parallel to the stringers. This is similar to the observations made by Spitzig and Sober [26] and Erturk et al. [27].

The low fracture strains with the 1144 annealed material in the collar test suggests that the fracture process is largely dominated by the presence of sulphides. This is supported by the fact that spheroidizing or decarburizing the 1144 material had a much smaller influence on the fracture strains in the collar test, than with the 1045 or 1541 material.

The micrographs showing the fracture path in 1144 and 1045, Figures 13 and 14, suggest that because the inclusion spacing of 1144 is approximately equal to the ferrite grain size, the plastic zone at the crack tip is only required to expand to include one ferrite grain before coalescence between the crack tip and a neighbouring cavity occurs. In 1045 the inclusions are much further apart and the plastic zone at the crack tip expands to include

pearlite colonies before coalescence with voids ahead of the crack occurs. In essence the presence of numerous inclusions in 1144 allows the crack to propagate along the path of lower flow stress ie; the ferrite grains. In 1045 the larger inclusion spacing forces the crack to propagate through pearlite colonies to link large inclusion nucleated voids.

Figure 15 shows the fracture surface of the spheroidized 1045 steel in the collar test. Note the line below the surface of the collar which is considered to be associated with the instability. In this case the instability may well be caused by a cluster of inclusions lying just below the surface of the collar, see Fig. 16. No instability was observed with the spheroidized 1144 material in the collar test, and Fig. 17 shows a typical fracture surface.

From the micrograph of the shear fracture surface of the 1095 material in the compression test, Fig. 12b, it is evident that fracture has been caused by the linking of voids along directions of maximum shear stress. The strain path analysis, Table 6, shows that in the cylindrical 1095 samples the fracture strain corresponds closely with the strain at which tensile instabilities are predicted. This suggests that the onset of tensile instability is accompanied by a rapid acceleration of the damage, and consequently the post instability strain to fracture is small. The behaviour of the 1095 material in both the collar and tension tests is reported in [13], along with a discussion on shear band formation.

The fracture mechanism observed in all tests on the Fe-1.2P material was clearly intergranular. Figure 18 shows the intergranular cracks on the surface of a cylindrical test piece. A more detailed account of the fracture mechanisms in the Fe-1.2P material is to be found in Ref. [13].

4.3.3 Role of Surface Condition

Various accounts can be found in the literature on the rate of surface condition and surface properties in limiting the ductility of materials during upsetting.

Some aspects of surface condition were investigated in the present work and initially a number of experiments were conducted to compare the effect of drawn and machined surfaces on fracture strain. During the initial experiments on 1045 collar samples the drawn surface was preserved on the samples. Preliminary tests indicated that a drawing scratch was present in the rod, and as a result the remaining samples were reduced in diameter by 0.2 mm to remove the scratch. It was conjectured that this machining might have significantly increased the fracture strain by removal of longitudinally oriented damage at the surface of the sample resulting from the drawing operation. In order to test this hypothesis five spheroidized 1144 samples were tested, with both machined and drawn surfaces. The results of these tests are tabulated in Table 4. If the groups are compared using the students t-test with a 95% confidence interval, no significant difference is apparent. This indicates that the machining of the 1045 had no significant influence on the fracture strains observed in the collar tests and that it is reasonable to compare the results from these tests with the results from the other medium carbon steels.

It has been noted in the literature [28] that the drawing of wire using light reductions can result in better heading performance of the wire, i.e., fewer rejects due to cracking. The present study indicates that this improvement is not due to the improved surface finish after drawing. It has been noted in cases where the deformation zone geometry is characterized by a large H/L value, that the deformation zone might not extend to the centerline of the work piece. In such cases residual compressive stresses of the order of 1/3 the yield stress can be obtained at the surface. This suggests that improved heading after drawing is due to residual compressive stresses and that surface roughness effects are minor.

The second set of experiments used to study the effect of surface properties involved the decarburization of a thin (0.1 mm) layer on the surface of annealed 1045 and 1144 collar samples and comparing the fracture strains obtained with those for annealed samples. The results from these tests were again compared using the student's t-test at a 95% confidence

interval, and are contained in Table 4. It is clear that the surface decarburization significantly increases the strain to surface fracture in both steels. The increase in ductility is not as large as that observed for the spheroidized samples, and is of approximately the same magnitude for both steels. A limited quantitative metallographic examination of an 1144 sample was performed to assess the level of damage in the decarburized layer and the bulk material below the decaburized layer. All voiding was observed to occur at MnS particles and the area fraction of voids observed was 0.4% in the decarburized layer and 2.3% in the bulk material immediately below the decarburized layer.

The use of rimmed steels in forming operation where surface cracking is a limiting factor has been common in industry for a number of years [29]. The present results indicate that this improvement in formability is due to the lower rate at which voiding damage accumulates in the surface region. This lower damage rate is possibly due to two factors:

1) The lower flow stress of the ferrite which acts as a deterrent to void nucleation, by increasing the strain required before interface separation occurs.

2) The larger strains required in the ferrite before tensile instabilities, which accelerate damage accumulation occur.

3) The first factor mentioned is probably relatively insignificant in the present case because manganese sulphides, which are the prime nucleation sites for damage, generally have little or no cohesion to the matrix. Thus the presence of even small tensile stresses are sufficient to cause voiding.

Further discussion on the role of surface condition can be found in [13].

4.3.4 Fracture Criteria

An extended account of the fracture criteria applied to the various materials tested herein is available in Ref. [13]. However, in summary it is fair to say that no completely adequate criterion has emerged for either the ductile or more brittle materials.

As mentioned earlier, it is clear that the fracture data for all the upsetting tests on the ductile materials do not lie on a single fracture line, according to the proposal of Lee and Kuhn [1]. More recent Scandanavian work [30, 31] indicates that the slope of the fracture line can vary from -1/2, and that in strain paths close to plane strain the amount of inclusions on or close to the surface can exert a much stronger influence on the fracture strain than for strain paths well removed from plane strain. Our data is in qualitative agreement with these statements, but this is certainly not conclusive. The ductile fracture models of Refs. [3, 4, 24] do not fit our data. As discussed earlier it would appear that for each of these damage functions to reveal a constant value, the existence of a single fracture line is necessary.

Models which purport to predict the onset of instability strain, such as the one proposed by Thomason [20], are not always easy to check experimentally. The onset of instability is often missed and it is fracture strains which are determined, and even these are rather subjective. The suggestion in Ref. [15] that the post instability strain to fracture will be a function of the hydrostatic stress state and the proportion of second phases and inclusions in the matrix, is in quantitative agreement with the present results [13].

The hypothesis of a maximum shear stress criterion is not completely satisfactory, although there is some uncertainty in predicting the macroscopic stress state at fracture from the ε_θ-ε_z strain path data. Many tests would have to be conducted before some reliable stress values emerged. However, the simplicity of the criterion permits a ready check on available data.

A brittle fracture criterion, due to Murrel [32], was applied to the Fe-1.2P material. The model appeared incapable of predicting the fracture stress in the compression test, and would seem to be totally inappropriate for the collar test data because of the tensile nature of the stress states. Further discussion on these points is given in Ref. [13].

REFERENCES

1. Lee, P.W. and Kuhn, H.A., "Fracture in Cold Upset Forging - A Criterion and Model", Metall. Trans., Vol. 4, 1973, pp. 969-974.

2. Kuhn, H.A., Lee, P.W. and Ertürk, T., "A Fracture Criterion for Cold Forming", Trans. ASME, J. Eng. Mats. Tech., Vol. 95H, 1973, pp. 213-218.

3. Cockcroft, M.G. and Latham, D.J., "Ductility and the Workability of Metals", J. Inst. Metals, Vol. 96, 1968, pp. 33-39.

4. Oyane, M., "Criteria of Ductile Fracture Strain", Bull. JSME., Vol. 15, 1972, pp. 1507-1513.

5. Chandrasekaran, N., Brownrigg, A., Duncan, J.L., Embury, J.D. and Sowerby, R., "The Assessment of the Free Surface Strains and Stresses During the Upsetting of Circular Cylnders", Script. Met., Vol. 16, 1982, pp. 697-701.

6. Sowerby, R., O'Reilly, I., Chandrasekaran, N. and Dung, N.L., "Materials Testing for Cold Forging", Proc. of ASME's Winter Annual Meeting, Session in "Materials in Manufacturing", Boston, MA, November 1983.

7. Siddall, J.N., "Optimal Engineering Design - Principles and Applications", Marcel Dekker Inc., NY, 1982.

8. Kobayashi, S., "Deformation Characteristics and Ductile Fracture of 1040 Steel in Simple Upsetting of Solid Cylinders and Rings", Trans. ASME, J. Eng. Ind., Vol. 92B, 1970, pp. 391-399.

9. Chandrasekaran, N. and Sowerby, R., "The Characterization of Stress-Strain Data for Deep Drawing Quality Steels Using a Cubic Spline as the Interpolating Function", Internal Report, McMaster University, Ontario, Canada, 1983.

10. Dung, N.L. and Mahrenholtz, O., "Proc. Int. Conf. on Numerical Methods in Industrial Forming Processes", (Eds. J.F.T. Pittman et al.), Swansea, UK, pp. 187-196, Pineridge Press, 1982.

11. Dung, N.L., Newerla, A. and Marten, J., "FARM Finite Element Analysis of Rigid-Plastic Metal Forming - User's Manual", Institute of Mechanics, University of Hannover, Hannover, F.R. Germany, 1982.

12. Dung, N.L., "Finite Element Modelling of Upsetting Test", Metalforming Res. Report No. 83-013, McMaster University, July, 1983.

13. O'Reilly, I., "Flow and Fracture During Compression Tests of Cold Forging Steels", M.Eng. Thesis, McMaster University, Hamilton, Ontario, Canada, 1983.

14. Brownrigg, A., Duncan, J.L. and Embury, J.D., "Free Surface Ductility of Steels in Cold Forging", Internal Report, McMaster University, Hamilton, Ontario, Canada, 1979.

15. Thomason, P.F., "The Free Surface Ductility of Uniaxial Compression Specimens with Longitudinal Surface Defects", Int. J. Mech. Sci., Vol. 11, 1969, pp. 65-73.

16. Bridgman, P.W., "Studies in Large Plastic Flow and Fracture", MacGraw- Hill, 1952.

17. Ludwik, P., "Elemente der Technologischen Mechanik", Springer, Berlin, 1909.

18. Hill, R., "The Theory of the Yielding and Flow of Anisotropic Metals", Proc. Roy. Soc., Vol. 193A, 1948, pp. 281-297.

19. de Boor, C., "A Practical Guide to Splines", Springer-Verlag, 1978.

20. Thomason, P.F., "Tensile Plastic Instability and Ductile Fracture Criteria in Uniaxial Compression Tests", Int. J. Mech. Sci., Vol. 11, 1969, pp. 187-198.

21. Kudo, H. and Aoi, K., "Effect of Compression Test Condition Upon Fracturing of a Medium Carbon Steel", J. Japan Soc. Tech. Plasticity, Vol. 8, 1967, pp. 17-27.

22. LeRoy, G., Embury, J.D., Edwards, G. and Ashby, M.F., "A Model of Ductile Fracture Based on the Nucleation and Growth of Voids", Acta Met., Vol. 29, 1981, pp. 1509-1522.

23. Rice, J.R. and Tracey, D.M., "On the Ductile Enlargement of Voids in Triaxial Stress Fields", J. Mech. Phys. Solids, Vol. 17, 1969, pp. 201-217.

24. McClintock, F.A., "A Criterion for Ductile Fracture by the Growth of Holes", J. Appl. Mech., Vol. 35, 1968, pp. 363-371.

25. Brown, L.M. and Embury, J.D., in "Proc. 3rd Int. Conference on Strengths of Metal and Alloys", Cambridge University, UK, 1973, pp. 164-174.

26. Spitzig, W.A. and Sober, R.J., "Influence of Sulfide Inclusions and Pearlite Content on the Mechanical Properties of Hot-Rolled Carbon Steels", Met. Trans., Vol. 12A, 1981, pp. 281-291.

27. Erturk, T., Otto, W.L. and Kuhn, H.A., "Anisotropy of Ductile Fracture in Hot-rolled Steel Plates - an Application of the Upset Test", Met. Trans., Vol. 5A, 1974, pp. 2157-2159.

28. Patterson, M.S., in "Experimental Rock Deformation - The Brittle Field", Springer-Verlag, 1978.

29. Gill, F.L. and Baldwin, W.M., "Proper Wire Drawing Improves Cold Heading", Metal Progress, Vol. 85, Feb. 1964, pp. 83-85.

30. Kivivouri, S. and Sulonen, M., "Formability Limits and Fracturing Modes of Uniaxial Compression Specimens", CIRP Annals., Vol. 27, 1978, pp. 141-145.

31. Lahti, I. and Sulonen, M., "The Influence of Non-Metallic Inclusions on Cold-Upsettability of Low Carbon Steels", Scand. J. Met., Vol. 11, 1982, pp. 1-8.

32. Pierce, D., Asaro, R.J. and Needleman, A., "An Analysis of Non-uniform and Localised Deformation in Ductile Single Crystals", Acta Metall., Vol. 30, 1982, pp. 1087-1119.

Table 1

Chemical Composition of Test Materials (w/o)

Material	C	Mn	S	P	Fe
1045	0.473	0.76	0.007	-	Balance
1144	0.444	1.36	0.249	-	Balance
1541	0.382	1.63	0.021	-	Balance
1095	0.832	0.43	0.022	-	Balance
Fe-1.2P	0.005	0.032	0.001	1.2	Balance

Table 2

Mechanical Properties of the Test Materials

Material	Heat Treatment	σ_y (MPa)	σ_f (MPa)	$\bar{\varepsilon}_f$	A (MPa)	n
1045	a	393	1047	0.73	1049	0.18
	s	340	987	1.13	900	0.25
	d	350	1055	0.75	1055	0.19
1144	a	437	999	0.55	1091	0.14
	s	374	857	0.82	891	0.23
	d	460	1021	0.56	1176	0.19
1541	a	448	1283	0.95	1256	0.20
	s	370	1152	1.02	1162	0.28
	d	489	1231	1.00	1231	0.19
1095	h.r.	585	1221	0.20	1585	0.13
Fe-1.2P	a.q.	400	1355	1.28	1306	0.23

a - annealed

s - spheroidized

d - surface decarburized

h.r. - hot rolled

a.q. - annealed and quenched

Table 3

Cylindrical Compression Tests Between Rough Platens

Material	Heat Treatment	ε_θ	$-\varepsilon_z$	$\bar{\varepsilon}$
1045	a	0.71	0.62	0.89
	s+	0.93	0.75	1.18
	d+	1.04	0.86	1.20
1144	a	0.48	0.44	0.60
	s	0.52	0.51	0.67
	d	0.49	0.46	0.64
1541	a	0.77	0.58	0.78
	s	0.69	0.56	0.82
	d	0.77	0.58	0.82
1095	h.r.	0.40	0.42	0.64
	h.r.*	0.59	0.74	0.79
Fe-1.2P	a.q.	0.29	0.40	0.41
	a.q.*	0.64	0.13	0.13

a - annealed
s - spheroidized
d - decarburized
h.r. - hot rolled
a.q. - annealed and quenched

+ no fracture obtained
* smooth platens and a teflon lubricant at 10% height decrements

Table 4

Collar Tests - Fracture Data

Material	Heat Treatment	#Tests	ε_θ	s_θ	$-\varepsilon_z$	s_z	$\bar{\varepsilon}$	Comments
1045	a	7	0.32	0.035	0.12	0.027	0.33	Differences are
	s	10	0.59	0.050	0.26	0.030	0.59	significant at
	d	9	0.39	0.038	0.17	0.019	0.39	95% C.I.
1144	a	19	0.082	0.021	0.024	0.010	0.084	Differences are
	s	15	0.14	0.017	0.040	0.012	0.14	significant at
	d	15	0.12	0.010	0.039	0.010	0.12	95% C.I.
1541	a	2	0.18	-	0.039	-	0.19	indicates same
	s	2	0.26	-	0.88	-	0.26	trends as
	d	2	0.20	-	0.044	-	0.21	1045 & 1144
1095	h.r.	2	0.11	-	0.048	-	0.11	
Fe-1.2P	a.q.	1	0.026	-	0.003	-	0.028	
1144	s(1)	4	0.083	0.024	0.025	-	0.085	No significant
	s(2)	4	0.12	0.015	0.026	-	0.12	differences at
								95% C.I.
1045	a(3)	3	0.43	0.030	0.18	-	0.43	No significant
	a(4)	3	0.40	0.017	0.14	-	0.41	differences at
								95% C.I.

a - annealed s - spheroidized

h.r. - hot rolled a.q. - annealed and quenched

(1) - machined collar surface (2) - drawn collar surface

(3) - no flanges on ends (4) - flanges on ends

Table 5a

Inclusion Characteristics

Steel	Area Fraction %	Average Spacing (um)	Average Length (um)	Average Diameter (um)
1045	0.14	865	2.3	0.7
1144	3.80	39	29.	10.
1541	0.33	296	1.6	0.6
1095	0.42	642	1.9	0.6

Table 5b

Manganese Sulphide Size Distribution in 1144

Length (um)	0-2	2-5	5-10	10-20	>20
%	33.7	38.4	14.6	7.4	5.7
Width (um)	0-0.2	0.2-0.5	0.5-1.0	1.0-1.2	>2.0
%	0.2	24.1	55.1	14.1	6.1
L/W	0-2	2-3	3-4	4-5	>5
%	9.6	23.7	13.3	11.2	41.9

Table 6

Strain Path Analysis Results

Cylindrical Compression Tests

Material	Heat treatment	ε_{max}	σ_θ (MPa)	σ_z (MPa)	σ_m (MPa)	τ_{max} (MPa)	ε_{INS}	CCI (MPa)
1045	a	0.80	1098	163	421	549	0.58	545
	s	1.18	1076	432	502	538	0.70	637
	d	1.23	971	219	250	486	0.,50	835
1144	1	0.57	1046	85	377	543	0.51	300
	s	0.67	901	226	375	450	0.61	257
	d	0.59	1106	92	399	553	0.53	315
1541	a	0.78	1244	104	449	622	0.52	556
	s	0.82	1177	202	459	589	0.53	528
	d	0.82	1304	223	509	652	0.51	608
1095	h.r.	0.47	1237	-343	2967	790	0.47	431
	h.r.*	0.79	975	-798	59	886	0.79	420
Fe-1.2P	a.q.	0.41	662	-568	31	615	>0.41	109

CCI - Cockcroft Integral

a - annealed

s - spheroidized

d - decarburized

h.r. - hot rolled

a.q. - annealed and quenched

* - Lubricated compression test

Table 7

Strain Path Analysis Results

Collar Tests

Material	Heat treatment	$\bar{\varepsilon}_{max}$	σ_θ (MPa)	σ_z (MPa)	σ_m (MPa)	τ_{max} (MPa)	ε_{INS}	CCI (MPa)
1045	a	0.32	909	128	345	454	0.19	240
	s	0.59	810	63	291	405	0.25	363
	d	0.39	923	88	337	641	0.21	298
1144	a	0.084	849	194	348	425	>0.09	65
	s	0.14	626	145	256	313	>0.14	64
	d	0.12	860	185	348	430	>0.12	87
1541	a	0.19	1048	392	480	524	>0.19	130
	s	0.26	840	136	325	420	0.25	161
	d	0.21	1014	240	418	507	0.19	163
1095	h.r.	0.11	1260	145	468	630	>0.11	118
Fe-1.2P	a.q.	0.028	271	663	311	330	>0.028	0

CCI - Cockcroft Integral

a - annealed

s - spheroidized

d - decarburized

h.r. - hot rolled

a.q. - annealed and quenched

* - Lubricated compression test

Table 8: Fracture Data from the Upset Tests

Shown in Figure 2

TYPE OF TEST	FRACTURE STRAIN ε_f	COCKCROFT INTEGRAL	$\int_0^{\bar{\varepsilon}_f} \sigma_m \, d\bar{\varepsilon}$	$\int_0^{\bar{\varepsilon}_f} \sigma_m/\bar{\sigma} \, d\bar{\varepsilon}$	OYANE INTEGRAL $C_2 = \int^{\bar{\varepsilon}_f} (1 + 1/C_1 \, \sigma_m/\bar{\sigma}) \, d\varepsilon$		$\sigma_{\theta_{max}}$
					C_1 (Average)	C_2	
		MPa	MPa				MPa
1045 Steel							
Compression Tests							
B1	0.591	405.03	61.98	0.050	0.48	0.696	1087
B2	0.616	380.83	33.34	0.021	0.48	0.662	1019
B3	0.778	423.76	14.56	-0.010	0.48	0.756	1178
Punch Tests							
C1	0.457	441.97	43.26	0.011	0.48	0.481	1217
C2	0.583	246.27	-28.09	-0.052	0.48	0.474	1219
Collar Test							
A	0.218	196.55	62.82	0.080	0.48	0.385	996

Table 9: Integrals Based on Linear Strain Paths

STRAIN RATIO α	FRACTURE STRAIN $\bar{\varepsilon}_f$	COCKCROFT INTEGRAL $\int_0^{\bar{\varepsilon}_f} \sigma^* \, d\bar{\varepsilon}$ MPa	$\int_0^{\bar{\varepsilon}_f} \sigma_m \, d\bar{\varepsilon}$ MPa	OYANE INTEGRAL $\int_0^{\varepsilon_f} (1 + 1/C_1 \, \sigma_m/\bar{\sigma}) \, d\bar{\varepsilon}$
-5000.000	0.346	364.48	-182.22	0.763
-1000.000	0.346	364.48	-182.15	0.762
-200.000	0.346	364.48	-181.78	0.762
-100.000	0.346	364.48	-181.33	0.761
-15.500	0.347	364.55	-176.20	0.749
-5.500	0.352	365.13	-164.31	0.726
-3.500	0.361	366.24	-152.60	0.707
-2.643	0.374	367.81	-140.99	0.693
-2.167	0.390	369.75	-129.41	0.682
-1.864	0.410	371.97	-117.79	0.674
-1.654	0.433	374.39	-106.08	0.669
-1.500	0.458	376.93	-094.23	0.666
-1.382	0.485	379.54	-82.23	0.665
-1.289	0.514	382.17	-70.07	0.667
-1.214	0.544	384.80	-57.72	0.669
-1.152	0.576	387.40	-435.20	0.673
-1.100	0.608	389.96	-32.50	0.677
-1.056	0.642	392.46	-19.62	0.683
-1.017	0.676	394.90	-6.58	0.689
-0.984	0.710	397.28	6.62	0.696
-0.955	0.745	39.59	19.98	0.703
-0.929	0.781	401.83	33.49	0.711
-0.905	-0.817	404.01	47.13	0.719
-0.850	0.924	410.05	87.87	0.745
-0.800	1.058	416.75	138.92	0.780
-0.750	1.249	425.12	212.56	0.832
-0.700	1.539	435.92	326.94	0.914
-0.650	2.030	450.63	525.93	1.057

APPENDIX

As an example for the use of the finite element package FARM (Finite Element Analysis of Rigid-Plastic Metal Forming) [11], the calculation of a compression test (d_o = 14 mm and h_o = 21 mm) is performed. Due to symmetry, only one quarter of the cylindrical specimen is considered using a mesh of 100 identical quadrilateral elements. The nodes of the FE mesh are numbered in such a manner that the mesh is generated automatically and the storage is reduced, see Fig. 19. As a model for a strain-hardening material (1045 annealed steel), a yield curve described by

$$\bar{\sigma} = A\,(B + \bar{\varepsilon})^n$$

with $Y_o = A\,(B)^n$ when $\bar{\varepsilon} = 0$

is adopted. This stress-strain relation is rate-independent, hence the results do not depend on punch velocity. Hence for convenience the relative punch velocity is taken as unity, i.e. all nodes of the boundary 2 have the prescribed velocity $v_z/v_o = -1$, where v_o is the true punch velocity in a practical engineering situation. Because of symmetry, two other prescribed velocity boundary conditions can be given to the boundaries 1 and 4; i.e.,the velocity component $v_r/v_o = 0$ for every node of the boundary 1, and the velocity component $v_z/v_o = 0$ for every node of the boundary 4, see Fig. 19(a).

The computation is carried out using incremental deformation steps corresponding to reduction in the height of the cylinder of 2% of its initial value. The frictional condition described by a friction factor m = 1, to simulate the compression test between two rough flat platens. In this case, the free surface of the specimen bulges during the forming process, so that there are some nodes of the boundary 3 which will reach the die. Therefore, the contact problem has to be considered along the boundary 3. To illustrate the contact problem the node No. 221 is chosen, in this case the component z of every node of the boundary 3 must be equal or less than the component of node No. 221 during the process. If any node of the boundary 3 has a coordinate z which is larger than z of node 221, this indicates overlapping between the

die and specimen in the numerical solution. This is not allowed and the condition of this node is modified so that it now lies at the compression platens.

All the geometrical and topological data are entered in the FE package for performing the calculations on the data. As output of the calculation, one obtains step- by-step the information of the nodal velocities and forces, the stress field (Y, σ_r, σ_z, σ_θ, σ_{rz}, σ_m ...) and the strains ($\dot{\varepsilon}_r$, $\dot{\varepsilon}_z$, $\dot{\varepsilon}_\theta$, $\dot{\varepsilon}_{rz}$, equivalent strain rate $\bar{\dot{\varepsilon}}$, and equivalent strain $\bar{\varepsilon}$). Note that the stresses and strains are assumed to be constant in each quadrilateral element of the FE mesh because of the linear formulation [10, 11]. After each deformation step of 2% reduction in height, the nodal displacements are also determined in form of new nodal coordinates.

The input and output data are illustrated in this Appendix for the calculation of the first deformation step of the compression test. All of the output data are related to the initial velocity v_o or the initial yield stress Y_o. In this first deformation step the specimen has the initial geometry (d_o, h_o), the various quantities are calculated after a reduction in height of 2%.

The technical details of the finite element package FARM can be found in Refs. [10, 11].

INPUT DATA

TOPOLOGICAL DATA FOR FE MESH WITH 100 QUADRILATERAL ELEMENTS AND 221 NODES (NODE NUMBER BEGINS WITH No. 1)

```
2   1   0   1   0   2
1 100 221 221   0
1   1
4 100   1   1
10  10   1
```

NUMBERING THE NODES OF 100 ELEMENTS AFTER AN AUTOMATIC GENERATION OF FE MESH.

Nodes of Element No. 1.

1	2	12	22	23	2	3	13	23	24	3	4	14	24	25	4	5	15	25	26
5	6	16	26	27	6	7	17	27	28	7	8	18	28	29	8	9	19	29	30
9	10	20	30	31	10	11	21	31	32	22	23	33	43	44	23	24	34	44	45
24	25	35	45	46	25	26	36	46	47	26	27	37	47	48	27	28	38	48	49
28	29	39	49	50	29	30	40	50	51	30	31	41	51	52	31	32	42	52	53
43	44	54	64	65	44	45	55	65	66	45	46	56	66	67	46	47	57	67	68
47	48	58	68	69	48	49	59	69	70	49	50	60	70	71	50	51	61	71	72
51	52	62	72	73	52	53	63	73	74	64	65	75	85	86	65	66	76	86	87
66	67	77	87	88	67	68	78	88	89	68	69	79	89	90	69	70	80	90	91
70	71	81	91	92	71	72	82	92	93	72	73	83	93	94	73	74	84	94	95
85	86	96	106	107	86	87	97	107	108	87	88	98	108	109	88	89	99	109	110
89	90	100	110	111	90	91	101	111	112	91	92	102	112	113	92	93	103	113	114
93	94	104	114	115	94	95	105	115	116	106	107	117	127	128	107	108	118	128	129
108	109	119	129	130	109	110	120	130	131	110	111	121	131	132	111	112	122	132	133
112	113	123	133	134	113	114	124	134	135	114	115	125	135	136	115	116	126	136	137
127	128	138	148	149	128	129	139	149	150	129	130	140	150	151	130	131	141	151	152
131	132	142	152	153	132	133	143	153	154	133	134	144	154	155	134	135	145	155	156
135	136	146	156	157	136	137	147	157	158	148	149	159	169	170	149	150	160	170	171
150	151	161	171	172	151	152	162	172	173	152	153	163	173	174	153	154	164	174	175
154	155	165	175	176	156	156	166	176	177	156	157	167	177	178	157	158	168	178	179
169	170	180	190	191	170	171	181	191	192	171	172	182	192	193	172	173	183	193	194
173	174	184	194	195	174	175	185	195	196	175	176	186	196	197	176	177	187	197	198
177	178	188	198	199	178	179	189	199	200	190	191	201	211	212	191	192	202	212	213
192	193	203	213	214	193	194	204	214	215	194	195	205	215	216	195	196	206	216	217
196	197	207	217	218	197	198	208	218	219	198	199	209	219	220	199	200	210	220	221

Nodes of Element No. 97

Nodes of Element No. 100

INPUT OF THE INITIAL GEOMETRY

```
      11   0

  1   11    0.0000    0.0000    0.0000    1.0500
 22   32     .7000    0.0000    0.0000    1.0500
 43   53    1.4000    0.0000    0.0000    1.0500
 64   74    2.1000    0.0000    0.0000    1.0500
 85   95    2.8000    0.0000    0.0000    1.0500
106  116    3.5000    0.0000    0.0000    1.0500
127  137    4.2000    0.0000    0.0000    1.0500
148  158    4.9000    0.0000    0.0000    1.0500
169  179    5.6000    0.0000    0.0000    1.0500
190  200    6.3000    0.0000    0.0000    1.0500
211  221    7.0000    0.0000    0.0000    1.0500
```

CALCULATED NODAL COORDINATES R AND Z

(ONLY COORDINATES OF EDGE NODES ARE GIVEN)

Coordinates R and Z of Node No. 1

```
0.          0.          0.          .105E+01    0.          .210E+01    0.          .315E+01    0.          .420E+01
0.          .525E+01    0.          .630E+01    0.          .735E+01    0.          .840E+01    0.          .945E+01
0.          .105E+02    0.          0.          0.          0.          0.          0.          0.          0.
0.          0.          0.          0.          0.          0.          0.          0.          0.          0.
0.          0.           .700E+00   0.           .700E+00   .105E+01     .700E+00   .210E+01     .700E+00   .315E+01
 .700E+00   .420E+01     .700E+00    .525E+01    .700E+00    .630E+01    .700E+00    .735E+01    .700E+00    .840E+01
 .700E+00   .945E+01     .700E+00    .105E+02    0.          0.          0.          0.          0.          0.
0.          0.          0.          0.          0.          0.          0.          0.          0.          0.
0.          0.          0.          0.           .140E+01   0.           .140E+01    .105E+01    .140E+01    .210E+01
 .140E+01   .315E+01     .140E+01    .420E+01    .140E+01    .525E+01    .140E+01    .630E+01    .140E+01    .735E+01
 .140E+01   .840E+01     .140E+01    .945E+01    .140E+01    .105E+02    0.          0.          0.          0.
0.          0.          0.          0.          0.          0.          0.          0.          0.          0.
0.          0.          0.          0.          0.          0.           .210E+01   0.           .210E+01    .105E+01
 .210E+01   .210E+01     .210E+01    .315E+01    .210E+01    .420E+01    .210E+01    .525E+01    .210E+01    .630E+01
 .210E+01   .735E+01     .210E+01    .840E+01    .210E+01    .945E+01    .210E+01    .105E+02    0.          0.
0.          0.          0.          0.          0.          0.          0.          0.          0.          0.
0.          0.          0.          0.          0.          0.          0.          0.           .280E+01   0.
 .280E+01   .105E+01     .280E+01    .210E+01    .280E+01    .315E+01    .280E+01    .420E+01    .280E+01    .525E+01
 .280E+01   .630E+01     .280E+01    .735E+01    .280E+01    .840E+01    .280E+01    .945E+01    .280E+01    .105E+02
0.          0.          0.          0.          0.          0.          0.          0.          0.          0.
0.          0.          0.          0.          0.          0.          0.          0.          0.          0.
 .350E+01   0.           .350E+01    .105E+01    .350E+01    .210E+01    .350E+01    .315E+01    .350E+01    .420E+01
 .350E+01   .525E+01     .350E+01    .630E+01    .350E+01    .735E+01    .350E+01    .840E+01    .350E+01    .945E+01
 .350E+01   .105E+02     0.          0.          0.          0.          0.          0.          0.          0.
0.          0.          0.          0.          0.          0.          0.          0.          0.          0.
0.          0.           .420E+01   0.           .420E+01    .105E+01    .420E+01    .210E+01    .420E+01    .315E+01
 .420E+01   .420E+01     .420E+01    .525E+01    .420E+01    .630E+01    .420E+01    .735E+01    .420E+01    .840E+01
 .420E+01   .945E+01     .420E+01    .105E+02    0.          0.          0.          0.          0.          0.
0.          0.          0.          0.          0.          0.          0.          0.          0.          0.
0.          0.          0.          0.           .490E+01   0.           .490E+01    .105E+01    .490E+01    .210E+01
 .490E+01   .315E+01     .490E+01    .420E+01    .490E+01    .525E+01    .490E+01    .630E+01    .490E+01    .735E+01
 .490E+01   .840E+01     .490E+01    .945E+01    .490E+01    .105E+02    0.          0.          0.          0.
0.          0.          0.          0.          0.          0.          0.          0.          0.          0.
0.          0.          0.          0.          0.          0.           .560E+01   0.           .560E+01    .105E+01
 .560E+01   .210E+01     .560E+01    .315E+01    .560E+01    .420E+01    .560E+01    .525E+01    .560E+01    .630E+01
 .560E+01   .735E+01     .560E+01    .840E+01    .560E+01    .945E+01    .560E+01    .105E+02    0.          0.
0.          0.          0.          0.          0.          0.          0.          0.          0.          0.
0.          0.          0.          0.          0.          0.          0.          0.           .630E+01   0.
 .630E+01   .105E+01     .630E+01    .210E+01    .630E+01    .315E+01    .630E+01    .420E+01    .630E+01    .525E+01
 .630E+01   .630E+01     .630E+01    .735E+01    .630E+01    .840E+01    .630E+01    .945E+01    .630E+01    .105E+02
0.          0.          0.          0.          0.          0.          0.          0.          0.          0.
0.          0.          0.          0.          0.          0.          0.          0.          0.          0.
 .700E+01   0.           .700E+01    .105E+01    .700E+01    .210E+01    .700E+01    .315E+01    .700E+01    .420E+01
 .700E+01   .525E+01     .700E+01    .630E+01    .700E+01    .735E+01    .700E+01    .840E+01    .700E+01    .945E+01
 .700E+01   .105E+02
```

Coordinates R and Z of Node No. 221

GIVEN DISTRIBUTION OF SCALAR POSITIVE FACTOR ϕ

```
      E   0
.1C0E+01  .1CCE+C1  .1C0E+C1  .1C0E+11  .100E+C1  .100E+01  .100E+01  .100E+01  .100E+01  .100E+01
.1C0E+01  .1CCE+C1  .1C0E+C1  .1C0E+11  .100E+01  .1C0E+01  .100E+01  .100E+C1  .100E+01  .1C0E+01
.1C0E+01  .1CCE+C1  .1C0E+C1  .1CCE+11  .100E+C1  .1C0E+01  .100E+01  .100E+01  .1C0E+01  .1CCE+01
.1C0E+01  .1CCE+C1  .1C0E+01  .100E+11  .1C0E+01  .100E+C1  .100E+01  .100E+01  .100E+01  .1C0E+01
.1C0E+01  .1CCE+C1  .1C0E+11  .1C0E+11  .100E+01  .100E+01  .100E+01  .100E+01  .100E+C1  .1CCE+01
.1C0E+01  .1CCE+C1  .1C0E+11  .1C0E+11  .100E+01  .1C0E+01  .100E+01  .100E+01  .100E+01  .100E+01
.1C0E+01  .1CCE+C1  .1C0E+C1  .1C0E+01  .1C0E+01  .100E+01  .100E+01  .100E+01  .100E+01  .100E+01
.1C0E+01  .1CCE+C1  .1C0E+C1  .1CCE+11  .1C0E+01  .100E+01  .100E+01  .100E+01  .100E+01  .1C0F+01
.1C0E+01  .1CCE+C1  .1C0E+C1  .1C0E+11  .1C0E+01  .100E+01  .10CF+01  .100E+01  .100E+01  .1C0F+01
.1C0E+01  .1C0E+C1  .1C0E+C1  .100E+11  .100E+01  .1C0E+01  .100E+01  .100E+01  .1C0E+01  .1C0F+01
```

NODAL FRICTION FACTORS m IN R AND Z DIRECTIONS

```
0.          0.          C.          C.          0.          0.          0.          0.          0.          0.
0.          0.          C.          0.          0.          0.          0.          0.          0.          0.
 .1C0E+01   0.          C.          C.          0.          0.          0.          0.          0.          0.
0.          0.          G.          G.          0.          0.          0.          0.          0.          0.
0.          0.          C.          C.          0.          0.          0.          0.          0.          0.
0.          0.          C.          C.          C.          0.          0.          0.          0.          0.
0.          0.           .1C0E+C1   C.          0.          0.          C.          0.          0.          0.
0.          0.          C.          0.          0.          0.          0.          0.          0.          0.
0.          0.          C.          C.          0.          0.          0.          0.          0.          0.
0.          0.          C.          C.          C.          0.          0.          0.          0.          0.
0.          0.          C.          C.           .100E+01   0.          0.          0.          0.          0.
0.          0.          C.          0.          0.          0.          0.          0.          0.          0.
0.          0.          C.          C.          0.          0.          0.          0.          0.          0.
0.          0.          G.          C.          0.          0.          0.          0.          0.          0.
0.          0.          C.          C.          0.          0.           .100E+01   0.          0.          0.
0.          0.          C.          0.          0.          0.          0.          0.          0.          0.
0.          0.          C.          0.          0.          0.          0.          0.          0.          0.
0.          0.          C.          C.          0.          0.          0.          0.          0.          0.
0.          0.          C.          C.          0.          0.          0.          0.           .100E+01   0.
0.          0.          C.          0.          0.          0.          0.          0.          0.          0.
0.          0.          C.          C.          0.          0.          0.          0.          0.          0.
0.          0.          G.          C.          0.          0.          0.          0.          0.          0.
0.          0.          C.          C.          0.          0.          0.          0.          0.          0.
 .1C0E+01   0.          C.          C.          0.          0.          0.          0.          0.          0.
0.          0.          C.          C.          0.          0.          0.          0.          0.          0.
0.          0.          0.          G.          0.          0.          0.          0.          0.          0.
0.          0.          0.          0.          0.          0.          0.          0.          0.          0.
0.          0.           .1C0E+C1   C.          0.          0.          0.          0.          0.          0.
0.          0.          0.          C.          0.          0.          0.          0.          0.          0.
0.          0.          C.          C.          0.          0.          0.          0.          0.          0.
0.          0.          0.          0.          0.          0.          0.          0.          0.          0.
0.          0.          C.          C.           .100E+01   0.          0.          0.          0.          0.
0.          0.          C.          0.          0.          0.          0.          0.          0.          0.
0.          0.          C.          C.          0.          0.          0.          0.          0.          0.
0.          0.          0.          0.          0.          0.          0.          0.          0.          0.
0.          0.          C.          C.          0.          0.           .100E+01   0.          0.          0.
0.          0.          C.          C.          0.          0.          0.          0.          0.          0.
0.          0.          C.          0.          0.          0.          0.          0.          0.          0.
0.          0.          C.          C.          0.          0.          0.          0.           .1C0E+01   0.
0.          0.          C.          C.          0.          0.          0.          0.          0.          0.
0.          0.          C.          C.          0.          0.          0.          0.          0.          0.
0.          0.          C.          C.          0.          0.          0.          0.          0.          0.
 .1C0E+01   0.
```

Friction Factors of Node No. 221

34 DEFORMATION STEPS WITH 2% REDUCTION IN EACH STEP

AND MATERIAL DATA

```
 100  34   1  .680
* STEEL 1045 ANNEALED
   1   .105E+02  .100E+01  .100E-03  .300E-01   .142E+00  .100E-03
```

VELOCITY BOUNDARY CONDITIONS OF BOUNDARIES NO. 1, 2 AND 4

$V_r/V_0 = 0$

```
11   1  0.0000   1   2   3   4   5   6   7   8   9  10  11
11   2 -1.0000  11  32  53  74  95 116 137 158 179 200 221
11   2  0.0000   1  22  43  64  85 106 127 148 169 190 211
```

Nodes of Boundary 1

BOUNDARIES OF THE MESH WITH THEIR NODES

Boundary Number

```
11   1   1   2   3   4   5   6   7   8   9  10  11
11   2 221 200 179 158 137 116  95  74  53  32  11
11   3 211 212 213 214 215 216 217 218 219 220 221
11   4   1  22  43  64  85 106 127 148 169 190 211
```

END OF INPUT DATA

OUTPUT

OUTPUT DATA OF THE FIRST DEFORMATION STEP

CALCULATED STRAIN RATES AND STRESSES OF EACH ELEMENT

Element Number

	$\dot{\varepsilon}_r/v_0$	$\dot{\varepsilon}_z/v_0$	$\dot{\varepsilon}_\theta/v_0$	$\sqrt{2}\dot{\varepsilon}_{rz}/v_0$	σ_r/Y_0	σ_z/Y_0	σ_θ/Y_0	$\sqrt{2}\sigma_{rz}/Y_0$
1	.773E-01	-.155E+00	.7t9E-01	.275E-03	-.153E+00	-.115E+01	-.154E+00	.119E-02
2	.749E-01	-.15CE+C0	.741E-01	.116E-02	-.147E+00	-.115E+01	-.151E+00	.474E-02
3	.707E-01	-.142E+00	.694E-01	.166E-02	-.138E+00	-.114E+01	-.144E+00	.782E-02
4	.b49E-01	-.130E+00	.633E-01	.215E-02	-.126E+00	-.113E+01	-.135E+00	.111E-01
5	.584E-01	-.117E+00	.567F-01	.284E-02	-.114E+00	-.112E+01	-.124E+00	.163E-01
6	.516E-01	-.103E+C0	.499E-01	.265E-02	-.141E+00	-.115E+01	-.152E+00	.172E-01
7	.4b5E-01	-.932E-01	.457E-01	.319E-02	-.139E+00	-.119E+01	-.195E+00	.236E-01
8	.420E-01	-.843E-01	.405E-01	.414E-02	-.497E+00	-.150E+01	-.509E+00	.321E-01
9	.337E-01	-.711E-01	.310E-01	.117E-01	-.842E+00	-.184E+01	-.867E+00	.149F+00
10	-.439E-01	.925E-01	-.8C0E-01	-.190E-01	-.242E+01	-.158E+01	-.265F+01	-.118E+C0
11	.760E-01	-.153E+00	.768E-01	.326E-03	-.152E+00	-.115E+01	-.149E+00	.142E-02
12	.738E-01	-.148E+00	.743E-01	.140E-02.	-.148E+00	-.115E+01	-.14tE+00	.631E-02
13	.696E-01	-.140E+00	.700E-01	.238E-02	-.138E+00	-.114E+01	-.13tE+00	.113E-01
14	.b41E-01	-.129E+00	.642E-01	.3C0E-02	-.129E+00	-.113F+01	-.127E+00	.171E-01
15	.578E-01	-.11bE+00	.577E-01	.436E-02	-.114E+00	-.111E+01	-.115E+00	.251E-01
16	.520E-01	-.104E+00	.513E-01	.489E-02	-.117E+00	-.112E+01	-.121E+00	.314E-01
17	.463E-01	-.928E-01	.460E-01	.633E-02	-.199E+00	-.120E+01	-.200E+00	.454E-01
18	.396E-01	-.810E-01	.407E-01	.739E-02	-.432E+00	-.142E+01	-.423E+00	.608E-01
19	.225E-01	-.532E-01	.283E-01	.111E-01	-.947E+00	-.193E+01	-.875E+00	.127E+00
20	-.255E-01	.648E-01	-.440E-01	-.711E-01	-.190E+01	-.121E+01	-.204E+01	-.529E+00
21	.738E-01	-.15CE+00	.7t0E-01	.313E-03	-.145E+00	-.114E+01	-.139E+00	.135E-02
22	.717E-01	-.14tE+00	.737E-01	.167E-02	-.138E+00	-.113E+01	-.129E+00	.763E-02
23	.679E-01	-.138E+00	.695E-01	.226E-02	-.131E+00	-.113E+01	-.124E+00	.138E-01
24	.628E-01	-.127E+00	.639E-01	.414E-02	-.114E+00	-.111E+01	-.108E+00	.212E-01
25	.572E-01	-.115E+00	.577E-01	.538E-02	-.133E+00	-.110E+01	-.100E+00	.306E-01
26	.517E-01	-.104E+C0	.519E-01	.670E-02	-.987E-01	-.110E+01	-.999E-01	.431E-01
27	.457E-01	-.920E-01	.4t0E-01	.855E-02	-.177E+00	-.117E+01	-.175E+00	.618E-01
28	.3b5E-01	-.766E-01	.395E-01	.967E-02	-.401E+00	-.138E+01	-.375E+00	.753E-01
29	.182E-01	-.445E-01	.251E-01	-.165E-02	-.821E+00	-.176E+01	-.71tE+00	-.248E-01
30	-.954E-02	.4CCE-01	-.318E-01	-.959E-01	-.151E+01	-.113E+01	-.167E+01	-.718E+00
31	.709E-01	-.14tE+C0	.750E-01	.363E-03	-.131E+00	-.112E+01	-.112E+00	.166E-02
32	.691E-01	-.142E+C0	.728E-01	.159E-02	-.128E+00	-.112E+01	-.111E+00	.746E-02
33	.657E-01	-.135E+00	.688E-01	.289E-02	-.112E+00	-.110E+01	-.970E-01	.143E-01
34	.613E-01	-.125E+00	.634F-01	.436E-02	-.134E+00	-.110E+01	-.929E-01	.222E-01
35	.564E-01	-.114E+C0	.574E-01	.565E-02	-.827E-01	-.108E+01	-.764E-01	.330E-01
36	.510E-01	-.103E+C0	.515E-01	.763E-02	-.926E-01	-.109E+01	-.896E-01	.495E-01
37	.443E-01	-.903E-01	.457E-01	.928E-02	-.154E+00	-.115E+01	-.144E+00	.693E-01
38	.345E-01	-.732E-01	.383E-01	.672E-02	-.345E+00	-.132E+01	-.310E+00	.611E-01
39	.191E-01	-.431E-01	.234E-01	-.110E-01	-.675E+00	-.162E+01	-.610E+00	-.182E+00
40	.348E-02	.146E-01	-.229E-01	-.117E+C0	-.121E+01	-.109E+01	-.140E+01	-.787E+00
41	.675E-01	-.141E+00	.737E-01	.249E-03	-.116E+00	-.113E+01	-.868E-01	.118E-02
42	.660E-01	-.139E+C0	.716E-01	.140E-02	-.107E+00	-.109E+01	-.797E-01	.679E-02
43	.631E-01	-.131E+00	.678E-01	.257E-02	-.103E+00	-.109E+01	-.791E-01	.131E-01
44	.594E-01	-.122E+C0	.638E-01	.417E-02	-.797E-01	-.107E+01	-.613E-01	.222E-01
45	.552E-01	-.112E+C0	.571E-01	.584E-02	-.792E-01	-.107E+01	-.690E-01	.346E-01
46	.499E-01	-.101E+00	.513E-01	.790E-02	-.741E-01	-.107E+01	-.651E-01	.519E-01
47	.430E-01	-.885E-01	.452E-01	.857E-02	-.139E+00	-.113F+01	-.121E+00	.644E-01
48	.339E-01	-.716E-01	.374E-01	.334E-02	-.273E+00	-.126E+01	-.240E+C0	.302E-01
49	.224E-01	-.456E-01	.229E-01	-.200E-01	-.533E+00	-.148E+01	-.532E+00	-.275E+00
50	.158E-01	-.528E-03	-.153E-01	-.131E+C0	-.962E+C0	-.109E+01	-.119E+01	-.901E+CC
51	.637E-01	-.136E+C0	.723E-01	.236E-03	-.959E-01	-.107F+01	-.540E-01	.116E-02
52	.625E-01	-.133E+00	.7C3E-01	.134E-02	-.937E-01	-.107F+01	-.549E-01	.571E-02
53	.b03E-01	-.127E+00	.667E-01	.230E-02	-.775E-01	-.106E+01	-.439E-01	.121E-01
54	.572E-01	-.119E+C0	.620E-01	.3F0E-02	-.766E-01	-.106F+01	-.500E-01	.213F-01
55	.534E-01	-.110E+00	.566F-01	.611E-02	-.519E-01	-.104E+01	-.327E-01	.364E-01
56	.488E-01	-.998E-01	.509F-01	.778E-02	-.760E-01	-.107F+01	-.617E-01	.519E-01
57	.424E-01	-.873E-01	.448F-01	.715E-02	-.966E-01	-.109E+01	-.743E-01	.537E-01

Element Number

	$\dot{\varepsilon}_r/v_o$	$\dot{\varepsilon}_z/v_o$	$\dot{\varepsilon}_\theta/v_o$	$\sqrt{2}\dot{\varepsilon}_{rz}/v_o$	σ_r/Y_o	σ_z/Y_o	σ_θ/Y_o	$\sqrt{2}\sigma_{rz}/Y_o$
58	.347E-01	-.718E-01	.369E-01	-.467E-03	-.217E+00	-.121E+01	-.197E+00	-.434E-02
59	.207E-01	-.501E-01	.223E-01	-.259E-01	-.412E+00	-.135E+01	-.453E+00	-.317E+00
60	.265E-01	-.179E-01	-.851E-02	-.190E+00	-.757E+00	-.107E+01	-.101E+01	-.742E+00
61	.597E-01	-.133E+00	.708E-01	.179E-03	-.740E-01	-.105E+01	-.220E-01	.917E-03
62	.589E-01	-.128E+00	.688E-01	.938E-03	-.734E-01	-.104E+01	-.187E-01	.479E-02
63	.572E-01	-.123E+00	.655E-01	.210E-02	-.696E-01	-.105E+01	-.235E-01	.109E-01
64	.547E-01	-.116E+00	.610E-01	.363E-02	-.487E-01	-.103E+01	-.122E-01	.209E-01
65	.513E-01	-.107E+00	.559E-01	.572E-02	-.583E-01	-.104E+01	-.297E-01	.355E-01
66	.473E-01	-.979E-01	.505E-01	.765E-02	-.339E-01	-.102E+01	-.124E-01	.520E-01
67	.428E-01	-.873E-01	.445E-01	.575E-02	-.899E-01	-.109E+01	-.759E-01	.438E-01
68	.369E-01	-.736E-01	.367E-01	-.383E-02	-.137E+00	-.114E+01	-.137E+00	-.346E-01
69	.315E-01	-.558E-01	.242E-01	-.259E-01	-.317E+00	-.127E+01	-.398E+00	-.327E+00
70	.361E-01	-.337E-01	-.227E-02	-.110E+00	-.571E+00	-.106E+01	-.839E+00	-.740E+00
71	.595E-01	-.124E+00	.689E-01	.184E-03	-.579E-01	-.102E+01	.134E-01	.985E-03
72	.551E-01	-.122E+00	.672E-01	.731E-03	-.562E-01	-.102E+01	.101E-01	.392E-02
73	.539E-01	-.118E+00	.642E-01	.161E-02	-.449E-01	-.101E+01	.130E-01	.910E-02
74	.519E-01	-.112E+00	.600E-01	.310E-02	-.455E-01	-.102E+01	.297E-02	.191E-01
75	.492E-01	-.104E+00	.552E-01	.513E-02	-.251E-01	-.103E+01	.129E-01	.333E-01
76	.457E-01	-.958E-01	.500E-01	.680E-02	-.455E-01	-.103E+01	-.162E-01	.472E-01
77	.430E-01	-.874E-01	.443E-01	.583E-02	-.961E-02	-.100E+01	.232E-03	.444E-01
78	.407E-01	-.777E-01	.370E-01	-.549E-02	-.117E+00	-.113E+01	-.148E+00	-.470E-01
79	.368E-01	-.623E-01	.256E-01	-.334E-01	-.207E+00	-.117E+01	-.316E+00	-.326E+00
80	.444E-01	-.477E-01	.350E-02	-.993E-01	-.414E+00	-.105E+01	-.695E+00	-.682E+00
81	.513E-01	-.118E+00	.671E-01	.274E-03	-.411E-01	-.994E+00	.473E-01	.154E-02
82	.513E-01	-.117E+00	.656E-01	.375E-03	-.371E-01	-.994E+00	.443E-01	.213E-02
83	.505E-01	-.113E+00	.628E-01	.688E-03	-.341E-01	-.996E+00	.381E-01	.580E-02
84	.490E-01	-.108E+00	.589E-01	.220E-02	-.226E-01	-.991E+00	.351E-01	.136E-01
85	.469E-01	-.101E+00	.544E-01	.446E-02	-.243E-01	-.998E+00	.250E-01	.267E-01
86	.445E-01	-.940E-01	.494E-01	.544E-02	-.131E-02	-.982E+00	.336E-01	.386E-01
87	.422E-01	-.863E-01	.441E-01	.543E-02	-.220E-01	-.101E+01	-.703E-02	.419E-01
88	.437E-01	-.814E-01	.377E-01	-.191E-02	.351E-01	-.988E+00	-.139E-01	-.157E-01
89	.457E-01	-.733E-01	.274E-01	-.334E-01	-.203E+00	-.121E+01	-.360E+00	-.283E+00
90	.511E-01	-.595E-01	.865E-02	-.931E-01	-.257E+00	-.997E+00	-.541E+00	-.622E+00
91	.473E-01	-.113E+00	.652E-01	.352E-03	-.262E-01	-.969E+00	.753E-01	.208E-02
92	.476E-01	-.112E+00	.639E-01	-.629E-04	-.222E-01	-.970E+00	.749E-01	-.375E-03
93	.473E-01	-.110E+00	.613E-01	-.762E-05	-.180E-01	-.972E+00	.678E-01	-.466E-04
94	.465E-01	-.104E+00	.577E-01	.561E-03	-.140E-01	-.976E+00	.580E-01	.358E-02
95	.450E-01	-.985E-01	.535E-01	.137E-02	-.248E-02	-.973E+00	.548E-01	.926E-02
96	.430E-01	-.919E-01	.488E-01	.253E-02	.568E-02	-.972E+00	.481E-01	.183E-01
97	.410E-01	-.849E-01	.438E-01	.314E-02	.313E-01	-.956E+00	.542E-01	.239E-01
98	.407E-01	-.798E-01	.382F-01	.257E-02	.369E-01	-.974E+00	.151E-01	.217E-01
99	.506E-01	-.803E-01	.298E-01	-.147E-01	.838E-01	-.979E+00	-.852E-01	-.120E+00
100	.672E-01	-.819E-01	.140E-01	-.754E-01	-.314E+00	-.124E+01	-.647E+00	-.473E+00

EQUIVALENT STRAIN RATE $\bar{\dot{\varepsilon}}/v_o$ OF EACH ELEMENT

$\bar{\dot{\varepsilon}}/v_o$ of Element No. 1

.155E+00	.150E+00	.141E+00	.129E+00	.116E+00	.103E+00	.929E-01	.838E-01	.703E-01	.107E+00
.153E+00	.148E+00	.140E+00	.129E+00	.116E+00	.104E+00	.928E-01	.810F-01	.532E-01	.883E-01
.150E+00	.146E+00	.138E+00	.127E+00	.115E+00	.104E+00	.922E-01	.767E-01	.443E-01	.891E-01
.146E+00	.142E+00	.135E+00	.125E+00	.114E+00	.103E+00	.905E-01	.733E-01	.441E-01	.909E-01
.141E+00	.138E+00	.131E+00	.122E+00	.112E+00	.102E+00	.887E-01	.716E-01	.483E-01	.925E-01
.136E+00	.133E+00	.127E+00	.119E+00	.110E+00	.100E+00	.875E-01	.717E-01	.543E-01	.940E-01
.130E+00	.128E+00	.123E+00	.116E+00	.107E+00	.981E-01	.874E-01	.736E-01	.610E-01	.957E-01
.125E+00	.123E+00	.119E+00	.112E+00	.105E+00	.960E-01	.875E-01	.779E-01	.683E-01	.970E-01
.119E+00	.117E+00	.114E+00	.108E+00	.101E+00	.941E-01	.864E-01	.815E-01	.787E-01	.957E-01
.113E+00	.112E+00	.109E+00	.104E+00	.980E-01	.919E-01	.849E-01	.790E-01	.821E-01	.106E+00

$\bar{\dot{\varepsilon}}/v_o$ of Element No. 91

RELATIVE YIELD STRESS Y/Y_0 OF EACH ELEMENT

(ALL EQUAL 1.0 AT THE BEGINNING OF FORMING PROCESS)

.1C0E+01	.1C0E+01	.1C0E+01	.1C0E+01	.1C0E+01	.1C0E+01	.1C0E+01	.1C0E+01	.1C0E+01	.1C0E+01
.1C0E+01	.1C0E+01	.1C0E+01	.1C0E+01	.1C0E+01	.1C0E+01	.1C0E+01	.1C0E+01	.1C0E+01	.1C0E+01
.1C0E+01	.1C0E+01	.1C0E+01	.1C0E+01	.1C0E+01	.1C0E+01	.1C0E+01	.1C0E+01	.1C0E+01	.1C0E+01
.1C0E+01	.1C0E+01	.1C0E+01	.1C0E+01	.1C0E+01	.1C0E+01	.1C0E+01	.1C0E+01	.1C0E+01	.1C0E+01
.1C0E+01	.1C0E+01	.1C0E+01	.1C0E+01	.1C0E+01	.1C0E+01	.1C0E+01	.1C0E+01	.1C0E+01	.1C0E+01
.1C0E+01	.1C0E+01	.1C0E+01	.1C0E+01	.1C0E+01	.1C0E+01	.1C0E+01	.1C0E+01	.1C0E+01	.1C0E+01
.1C0E+01	.1C0E+01	.1C0E+01	.1C0E+01	.1C0E+01	.1C0E+01	.1C0E+01	.1C0E+01	.1C0E+01	.1C0E+01
.1C0E+01	.1C0E+01	.1C0E+01	.1C0E+01	.1C0E+01	.1C0E+01	.1C0E+01	.1C0E+01	.1C0E+01	.1C0E+01
.1C0E+01	.1C0E+01	.1C0E+01	.1C0E+01	.1C0E+01	.1C0E+01	.1C0E+01	.1C0E+01	.1C0E+01	.1C0E+01
.1C0E+01	.1C0E+01	.1C0E+01	.1C0E+01	.1C0E+01	.1C0E+01	.1C0E+01	.1C0E+01	.1C0E+01	.1C0E+01

CALCULATED DISTRIBUTION OF SCALAR-POSITIVE FACTOR ϕ/Y_0

.431E+01	.445E+01	.473E+01	.515E+01	.573E+01	.649E+01	.718E+01	.796E+01	.949E+01	.622E+01
.436E+01	.450E+01	.478E+01	.518E+01	.575E+01	.643E+01	.718E+01	.823E+01	.125E+02	.755E+01
.444E+01	.458E+01	.484E+01	.525E+01	.579E+01	.644E+01	.723E+01	.869E+01	.151E+02	.748E+01
.456E+01	.470E+01	.495E+01	.534E+01	.585E+01	.648E+01	.736E+01	.909E+01	.151F+02	.734E+01
.472E+01	.484E+01	.509E+01	.545E+01	.593E+01	.657E+01	.751E+01	.931E+01	.138E+02	.722E+01
.490F+01	.501E+01	.524E+01	.559E+01	.605E+01	.607E+01	.762E+01	.929E+01	.123E+02	.709F+01
.511E+01	.521E+01	.543E+01	.575E+01	.620E+01	.679E+01	.763E+01	.905E+01	.109E+02	.697E+01
.535E+01	.544E+01	.564E+01	.595E+01	.637E+01	.695E+01	.762E+01	.856E+01	.976E+01	.687E+01
.561E+01	.569E+01	.587E+01	.616E+01	.657E+01	.708E+01	.771E+01	.818E+01	.847E+01	.689E+01
.590E+01	.596E+01	.612E+01	.638E+01	.676E+01	.725E+01	.785E+01	.844E+01	.812F+01	.627F+01

ϕ/Y_0 of Element No. 91

CALCULATED NATURAL STRAIN $\bar{\varepsilon}$ OF EACH ELEMENT

$\bar{\varepsilon}$ of Element No. 1

.325E-01	.314E-01	.29cE-01	.272E-01	.244E-01	.216E-01	.195E-01	.176E-01	.148E-01	.225E-01
.321E-01	.311E-01	.294E-01	.270E-01	.243E-01	.218E-01	.195E-01	.170E-01	.112F-01	.185E-01
.315E-01	.306E-01	.289E-01	.267E-01	.242E-01	.218E-01	.194E-01	.161E-01	.930E-02	.187E-01
.307E-01	.298E-01	.283E-01	.2E2E-01	.239E-01	.216E-01	.190E-01	.154E-01	.926E-02	.191E-01
.297E-01	.289E-01	.279E-01	.257E-01	.236E-01	.213E-01	.186E-01	.150E-01	.102E-01	.194E-01
.286E-01	.279E-01	.267E-01	.251E-01	.231E-01	.210E-01	.184E-01	.151E-01	.114F-01	.197E-01
.274E-01	.269E-01	.259E-01	.243E-01	.226E-01	.206E-01	.184E-01	.155E-01	.129E-01	.201F-01
.262E-01	.257E-01	.249E-01	.235E-01	.220E-01	.202E-01	.184F-01	.164E-01	.144E-01	.204E-01
.249E-01	.246E-01	.239E-01	.227E-01	.213E-01	.198E-01	.181E-01	.171E-01	.165E-01	.209E-01
.237E-01	.235E-01	.229E-01	.219E-01	.207E-01	.193E-01	.178E-01	.166E-01	.172E-01	.223E-01

NODAL VELOCITY COMPONENTS V_r/V_0 AND V_z/V_0 FOR EDGE NODES AND MEAN STRESSES σ_m/Y_0 FOR MIDDLE NODES

v_r/v_0 and v_z/v_0 for Edge Node No. 1

.945E-11	-.787E-09	.659E-11	-.163E+00	.995E-11	-.321E+00	.127E-10	-.470E+00	.131E-10	-.607E+00
.128E-10	-.721E+00	.680E-11	-.838E+00	.105E-10	-.936E+00	.276E-10	-.103E+01	.155E-09	-.111E+01
.265E-10	-.110E+01	-.486E+00	0.	-.481E+00	0.	-.472E+00	0.	-.461E+00	0.
-.449E+00	0.	-.477E+00	0.	-.523E+00	0.	-.832E+00	0.	-.116E+01	0.
-.215E+01	0.	.547E-01	-.110E-08	.536E-01	-.162E+00	.513E-01	-.319E+00	.477E-01	-.467E+00
.432E-01	-.603E+00	.386E-01	-.725E+00	.337E-01	-.834E+00	.314E-01	-.932E+00	.273E-01	-.102E+01
.199E-01	-.108E+01	-.813E-01	-.133E+01	-.483E+00	0.	-.480E+00	0.	-.469E+00	0.
-.460E+00	0.	-.447E+00	0.	-.451E+00	0.	-.530E+00	0.	-.758E+00	0.
-.123E+01	0.	-.170E+01	0.	.108E+00	-.112E-08	.106E+00	-.159E+00	.102E+00	-.314E+00
.947E-01	-.466E+00	.859E-01	-.595E+00	.767E-01	-.716E+00	.683E-01	-.825E+00	.617E-01	-.922E+00
.525E-01	-.111E+01	.262E-01	-.105E+01	-.123E+00	-.100E+01	-.473E+00	0.	-.466E+00	0.
-.460E+00	0.	-.443E+00	0.	-.434E+00	0.	-.432E+00	0.	-.508E+00	0.
-.718E+00	0.	-.110E+01	0.	-.143E+01	0.	.160E+00	-.111E-08	.158E+00	-.156E+00
.151E+00	-.317E+00	.141E+00	-.459E+00	.128E+00	-.582E+00	.115E+00	-.703E+00	.103E+00	-.811E+00
.913E-01	-.917E+00	.740E-01	-.985E+00	.302E-01	-.103E+01	-.141E+00	-.100E+01	-.455E+00	0.
-.452E+00	0.	-.438E+00	0.	-.431E+00	0.	-.412E+00	0.	-.423E+00	0.
-.481E+00	0.	-.653E+00	0.	-.904E+00	0.	-.123E+01	0.	.210E+00	-.184E-08
.207E+00	-.151E+00	.198E+00	-.298E+00	.185E+00	-.438E+00	.169E+00	-.568E+00	.152E+00	-.687E+00
.136E+00	-.794E+00	.120E+00	-.888E+00	.939E-01	-.963E+00	.370E-01	-.101E+01	-.142E+00	-.100E+01
-.435E+00	0.	-.426E+00	0.	-.424E+00	0.	-.403E+00	0.	-.406E+00	0.
-.402E+00	0.	-.461E+00	0.	-.589E+00	0.	-.848E+00	0.	-.108E+01	0.
.258E+00	-.114E-08	.254E+00	-.146E+00	.244E+00	-.288E+00	.228E+00	-.424E+00	.209E+00	-.550E+00
.185E+00	-.668E+00	.169E+00	-.773E+00	.147E+00	-.865E+00	.114E+00	-.940E+00	.483E-01	-.990E+00
-.131E+00	-.110E+01	-.404E+00	0.	-.407E+00	0.	-.394E+00	0.	-.396E+00	0.
-.375E+00	0.	-.401E+00	0.	-.420E+00	0.	-.540E+00	0.	-.739E+00	0.
-.945E+00	0.	.303E+00	-.987E-09	.298E+00	-.140E+00	.287E+00	-.277E+00	.269E+00	-.409E+00
.248E+00	-.532E+00	.228E+00	-.646E+00	.202E+00	-.750E+00	.174E+00	-.841E+00	.126E+00	-.917E+00
.041E-01	-.972E+00	-.110E+00	-.100E+01	-.383E+00	0.	-.377E+00	0.	-.379E+00	0.
-.363E+00	0.	-.377E+00	0.	-.356E+00	0.	-.415E+00	0.	-.470E+00	0.
-.681E+00	0.	-.823E+00	0.	.344E+00	-.932E-09	.340E+00	-.134E+00	.328E+00	-.265E+00
.305E+00	-.392E+00	.286E+00	-.511E+00	.260E+00	-.623E+00	.223E+00	-.724E+00	.202E+00	-.816E+00
.159E+00	-.895E+00	.847E-01	-.957E+00	-.800E-01	-.100E+01	-.355E+00	0.	-.356E+00	0.
-.349E+00	0.	-.354E+00	0.	-.339E+00	0.	-.363E+00	0.	-.337E+00	0.
-.465E+00	0.	-.560E+00	0.	-.719E+00	0.	.383E+00	-.875E-09	.379E+00	-.128E+00
.366E+00	-.253E+00	.346E+00	-.375E+00	.321E+00	-.490E+00	.293E+00	-.598E+00	.264E+00	-.698E+00
.232E+00	-.789E+00	.186E+00	-.874E+00	.109E+00	-.943E+00	-.421E-01	-.100E+01	-.329E+00	0.
-.329E+00	0.	-.331E+00	0.	-.325E+00	0.	-.332E+00	0.	-.317E+00	0.
-.347E+00	0.	-.322E+00	0.	-.592E+00	0.	-.599E+00	0.	.419E+00	-.817E-09
.415E+00	-.121E+00	.402E+00	-.241E+00	.381E+00	-.359E+00	.355E+00	-.469E+00	.325E+00	-.574E+00
.294E+00	-.671E+00	.261E+00	-.761E+00	.219E+00	-.847E+00	.140E+00	-.932E+00	-.191E-02	-.100E+01
-.305E+00	0.	-.306E+00	0.	-.307E+00	0.	-.311E+00	0.	-.307E+00	0.
-.306E+00	0.	-.290E+00	0.	-.307E+00	0.	-.327E+00	0.	-.735E+00	0.
.452E+00	-.770E-09	.449E+00	-.115E+00	.435E+00	-.229E+00	.414E+00	-.341E+00	.387E+00	-.449E+00
.356E+00	-.551E+00	.324E+00	-.645E+00	.289E+00	-.734E+00	.248E+00	-.814E+00	.182E+00	-.898E+00
.503E-01	-.110E+01								

σ_m/Y_0 = -0.735 for Middle Node No. 210

NEW NODAL COORDINATES R AND Z AFTER 2% REDUCTION

.114E-11	-.165E-09	.138E-11	.102E+01	.209E-11	.203E+01	.266E-11	.305E+01	.275E-11	.407E+01
.270E-11	.510E+01	.143E-11	.612E+01	.222E-11	.715E+01	.579E-11	.818E+01	.326E-10	.922E+01
.957E-19	.103E+02	.353E+00	.525E+00	.350E+00	.154E+01	.350E+00	.263E+01	.350E+00	.369E+01
.350E+00	.472E+01	.350E+00	.573E+01	.350E+00	.683E+01	.350E+00	.788E+01	.350E+00	.893E+01
.350E+00	.997E+01	.711E+00	-.220E-09	.711E+00	.102E+01	.711E+00	.203E+01	.710E+00	.305E+01
.705E+00	.407E+01	.704E+00	.513E+01	.707E+00	.612E+01	.707E+00	.715E+01	.706E+00	.819E+01
.704E+00	.922E+01	.683E+00	.103E+02	.105E+01	.525E+00	.105E+01	.158E+01	.105E+01	.263E+01
.105E+01	.368E+01	.105E+01	.473E+01	.105E+01	.574E+01	.105E+01	.683E+01	.105E+01	.788E+01
.105E+01	.893E+01	.105E+01	.997E+01	.142E+01	-.236E-09	.142E+01	.102E+01	.142E+01	.203E+01
.142E+01	.305E+01	.142E+01	.408E+01	.142E+01	.510E+01	.141E+01	.613E+01	.141E+01	.716E+01

.141E+01	.819E+01	-.141E+01	.923E+01	.137E+01	.103E+02	.175E+01	.525E+00	.175E+01	.159E+01
.175E+01	.263E+01	.175E+01	.358E+01	.175E+01	.473E+01	.175E+01	.578E+01	.175E+01	.693E+01
.175E+01	.788E+01	.175E+01	.893E+01	.175E+01	.997E+01	.213E+01	-.233E-09	.213E+01	.102E+01
.213E+01	.204E+01	.213E+01	.306E+01	.213E+01	.408E+01	.212E+01	.510E+01	.212E+01	.613E+01
.212E+01	.718E+01	.212E+01	.819E+01	.211E+01	.923E+01	.207E+01	.103E+02	.245E+01	.525E+00
.245E+01	.158E+01	.245E+01	.263E+01	.245E+01	.368E+01	.245E+01	.473E+01	.245E+01	.578E+01
.245E+01	.683E+01	.245E+01	.788E+01	.245E+01	.893E+01	.245E+01	.997E+01	.284E+01	-.227E-09
.284E+01	.102E+01	.284E+01	.204E+01	.284E+01	.306E+01	.284E+01	.408E+01	.283E+01	.511E+01
.283E+01	.613E+01	.283E+01	.716E+01	.282E+01	.820E+01	.281E+01	.924E+01	.277E+01	.103E+02
.315E+01	.525E+00	.315E+01	.158E+01	.315E+01	.263E+01	.315E+01	.368E+01	.315E+01	.473E+01
.315E+01	.578E+01	.315E+01	.683E+01	.315E+01	.788E+01	.315E+01	.893E+01	.315E+01	.997E+01
.355E+01	-.218E-09	.355E+01	.102E+01	.355E+01	.204E+01	.355E+01	.306E+01	.354E+01	.408E+01
.354E+01	.511E+01	.354E+01	.614E+01	.353E+01	.717E+01	.352E+01	.820E+01	.351E+01	.924E+01
.347E+01	.113E+02	.385E+01	.525E+00	.385E+01	.158E+01	.385E+01	.263E+01	.385E+01	.368E+01
.385E+01	.473E+01	.385E+01	.578E+01	.385E+01	.683E+01	.385E+01	.788E+01	.385E+01	.893E+01
.385E+01	.997E+01	.426E+01	-.207E-09	.426E+01	.102E+01	.426E+01	.204E+01	.426E+01	.306E+01
.425E+01	.409E+01	.425E+01	.511E+01	.424E+01	.614E+01	.424E+01	.717E+01	.423E+01	.821E+01
.421E+01	.925E+01	.419E+01	.103E+02	.455E+01	.525E+00	.455E+01	.158E+01	.455E+01	.263E+01
.455E+01	.368E+01	.455E+01	.473E+01	.455E+01	.578E+01	.455E+01	.683E+01	.455E+01	.788E+01
.455E+01	.893E+01	.455E+01	.997E+01	.497E+01	-.196E-09	.497E+01	.102E+01	.497E+01	.204E+01
.496E+01	.307E+01	.496E+01	.409E+01	.495E+01	.512E+01	.495E+01	.615E+01	.494E+01	.718E+01
.493E+01	.821E+01	.492E+01	.925E+01	.488E+01	.103E+02	.525E+01	.525E+00	.525E+01	.158E+01
.525E+01	.263E+01	.525E+01	.368E+01	.525E+01	.473E+01	.525E+01	.578E+01	.525E+01	.683E+01
.525E+01	.788E+01	.525E+01	.893E+01	.525E+01	.997E+01	.568E+01	-.184E-09	.568E+01	.102E+01
.568E+01	.205E+01	.567E+01	.307E+01	.567E+01	.410E+01	.566E+01	.512E+01	.566E+01	.615E+01
.565E+01	.718E+01	.564E+01	.822E+01	.562E+01	.925E+01	.559E+01	.103E+02	.595E+01	.525E+00
.595E+01	.158E+01	.595E+01	.263E+01	.595E+01	.368E+01	.595E+01	.473E+01	.595E+01	.578E+01
.595E+01	.683E+01	.595E+01	.788E+01	.595E+01	.893E+01	.595E+01	.997E+01	.639E+01	-.172E-09
.629E+01	.112E+01	.638E+01	.215E+01	.638E+01	.307E+01	.637E+01	.410E+01	.637E+01	.513E+01
.633E+01	.616E+01	.635E+01	.719E+01	.635E+01	.822E+01	.633E+01	.925E+01	.630E+01	.103E+02
.665E+01	.525E+00	.665E+01	.158E+01	.665E+01	.263E+01	.665E+01	.368E+01	.665E+01	.473E+01
.665E+01	.578E+01	.665E+01	.683E+01	.665E+01	.788E+01	.665E+01	.893E+01	.665E+01	.997E+01
.709E+01	-.162E-09	.709E+01	.103E+01	.709E+01	.205E+01	.709E+01	.308E+01	.708E+01	.411E+01
.707E+01	.513E+01	.707E+01	.616E+01	.706E+01	.720E+01	.705E+01	.823E+01	.704E+01	.926E+01
.711E+01	.113E+02								

Coordinates R and Z of Node No. 221

RELATIVE NODAL FORCE COMPONENTS IN R AND Z DIRECTIONS

(FORCE/2nY$_0$)

-.199E-02	.112E+00	-.394E-02	.511E-14	-.639E-02	.187E-13	-.910E-02	.429E-13	-.110E-01	.466E-13
-.128E-01	.153E-12	-.791E-02	.144E-12	-.119E-01	.229E-12	-.251E-01	.194E-12	-.846E-01	.917E-13
-.382E-10	-.144E+00	-.555E-15	0.	-.444E-15	0.	0.	0.	-.133E-14	0.
-.444E-15	0.	-.888E-15	0.	-.888E-15	0.	-.178E-14	0.	-.355E-14	0.
.215E-05	0.	-.305E-09	.663E+00	-.297E-09	.711E-13	.387E-09	.103E-12	.277E-09	.215E-12
-.497E-09	-.140E-12	-.237E-10	-.593E-12	-.212E-09	.479E-12	-.143E-09	.361E-12	.598E-10	-.312E-12
.122E-08	.373E-13	-.283E+00	-.657E+00	.444E-15	0.	-.355E-14	0.	-.178E-14	0.
0.	0.	-.178E-14	0.	.178E-14	0.	.124E-13	0.	-.355E-14	0.
-.711E-14	0.	-.533E-14	0.	-.433E-08	.131E+01	-.966E-08	.284E-12	-.421E-09	-.263E-12
-.108E-07	-.183E-12	-.849E-08	-.497E-13	-.757E-08	-.149E-11	-.130E-07	-.243E-11	-.705E-08	-.190E-11
-.841E-08	-.141E-12	-.219E-08	-.793E-12	-.966E+00	-.113E+01	-.173E-13	0.	.169E-13	0.
.355E-14	0.	-.533E-14	0.	-.124E-13	0.	.711E-14	0.	.107E-13	0.
.355E-14	0.	.355E-14	0.	.107E-13	0.	.379E-07	.191E+01	.428E-07	-.494E-12
.568E-07	-.729E-12	.897E-07	-.120E-11	.819E-07	-.159E-11	.720E-07	-.146E-11	.100E-06	-.170E-11
.049E-07	-.609E-12	.360E-07	-.199E-11	.946E-07	-.544E-12	-.849E+00	-.156E+01	.213E-13	0.
-.711E-14	0.	.355E-14	0.	.107E-13	0.	.711E-14	0.	.178E-13	0.
.107E-13	0.	-.107E-13	0.	-.711E-14	0.	.533E-13	0.	.138E-06	.246E+01
.176E-06	-.351E-12	.294E-06	-.358E-12	.207E-06	-.125E-11	.255E-06	-.909E-12	.221E-06	-.344E-12
.213E-06	-.561E-11	.202E-06	-.784E-11	.213E-06	-.214E-11	.248E-06	-.379E-11	-.113E+01	-.197E+01
-.133E-13	0.	-.249E-13	0.	-.160E-13	0.	.107E-13	0.	.711E-14	0.

```
 .249E-13 0.          -.711E-14 0.          .142E-13 0.          -.213E-13 0.          -.355E-13 0.
 .144E-07  .296E+01   .314E-07 -.313E-12   .109E-06 -.675E-12 -.312E-07 -.384E-12 -.468E-07 -.370E-11
-.962E-07 -.295E-11   .565E-07 -.680E-11   .115E-06 -.514E-11 -.383E-07 -.491E-11  .135E-06 -.810E-12
-.141E+01 -.239E+01 -.115E-12 0.          -.515E-13 0.           .711E-14 0.          -.142E-13 0.
 .711E-14 0.           .213E-13 0.          .355E-13 0.          .213E-13 0.           .355E-13 0.
-.213E-13 0.           .597E-07  .341E+01   .230E-06 -.185E-12   .359E-06 -.101E-11   .345E-06 -.139E-11
 .380E-06 -.387E-11   .231E-06 -.348E-11   .734E-07 -.148E-11   .312E-06 -.373E-11   .345E-06 -.147E-11
 .134E-06 -.421E-11  -.173E+01 -.281E+01  -.959E-13 0.          -.568E-13 0.           .391E-13 0.
 .355E-14 0.          -.213E-13 0.          .213E-13 0.           .284E-13 0.           .924E-13 0.
 .213E-13 0.           .569E-13 0.          .391E-06  .380E+01   .736E-06  .711E-13   .797E-06 -.288E-11
 .763E-06 -.242E-12   .106E-05 -.190E-11   .970E-06  .146E-11   .542E-06 -.422E-11   .108E-05 -.439E-11
 .824E-06 -.370E-11   .764E-06 -.551E-11  -.194E+01 -.193E+01  -.200E-12 0.          -.101E-12 0.
-.249E-13 0.           .142E-13 0.          -.711E-14 0.           .426E-13 0.           .639E-13 0.
 .142E-13 0.           .497E-13 0.          .782E-13 0.           .532E-06  .417E+01   .974E-06  .284E-13
 .121E-05 -.134E-11   .164E-05 -.995E-12   .159E-05 -.526E-12   .129E-05 -.180E-11   .166E-05  .512E-12
 .838E-06 -.144E-11   .952E-06 -.988E-12   .117E-05 -.553E-11  -.226E+01 -.367E+01  -.268E-12 0.
-.110E-12 0.          -.391E-13 0.          -.711E-14 0.          -.711E-14 0.           0.          0.
 .497E-13 0.           .711E-13 0.          .121E-12 0.          -.142E-12 0.           .447E-06  .453E+01
 .100E-05  .142E-11   .531E-06 -.202E-11   .914E-06 -.398E-12   .895E-06 -.114E-12   .131E-05 -.378E-11
 .382E-06 -.735E-11   .908E-06 -.514E-11   .129E-05 -.212E-11   .142E-05 -.730E-11  -.255E+01 -.459E+01
-.423E-12 0.          -.103E-12 0.          -.284E-13 0.           .213E-13 0.           .568E-13 0.
 0.        0.           .426E-13 0.          .156E-12 0.           .128E-12 0.          -.568E-13 0.
-.225E-06  .231E+01  -.139E-05  .853E-12  -.759E-06 -.216E-11  -.650E-06 -.938E-12  -.584E-06 -.119E-11
-.187E-05 -.428E-11  -.111E-06 -.466E-11  -.195E-05 -.364E-11  -.130E-05 -.125E-11  -.144E-05 -.955E-11
-.134E+01 -.549E+01
```

Forces in R and Z Directions

of Node No. 220

TOTAL FORCES (IN R AND Z DIRECTIONS) ON EACH BOUNDARY (FORCE/$2\pi Y_0$)

```
-.175E+00 -.322E-11  -.141E+02 -.276E+02  -.134E+01 -.318E+01 -.199E-02  .276E+02
```

Forces on Boundary 2

(FORMING LOAD = FORCE IN Z DIRECTION ON BOUNDARY 2)

END OF THE FIRST DEFORMATION STEP

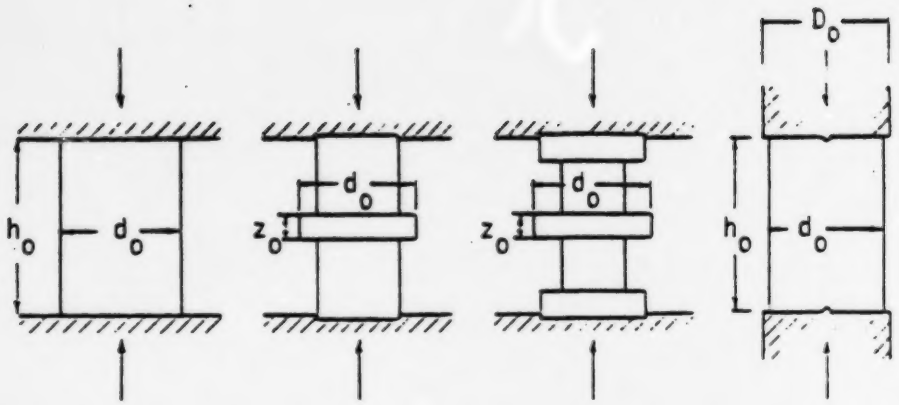

a) Compression Test
d_o = 10 mm
h_o = 15 mm

b) Collar Test
d_o = 15.6 mm
z_o = 3 mm

c) Collar Test
d_o = 12.5mm
z_o = 3 mm

d) Punch Test
D_o = 15 mm
d_o = 14 mm
h_o = 21 mm

FIG. 1

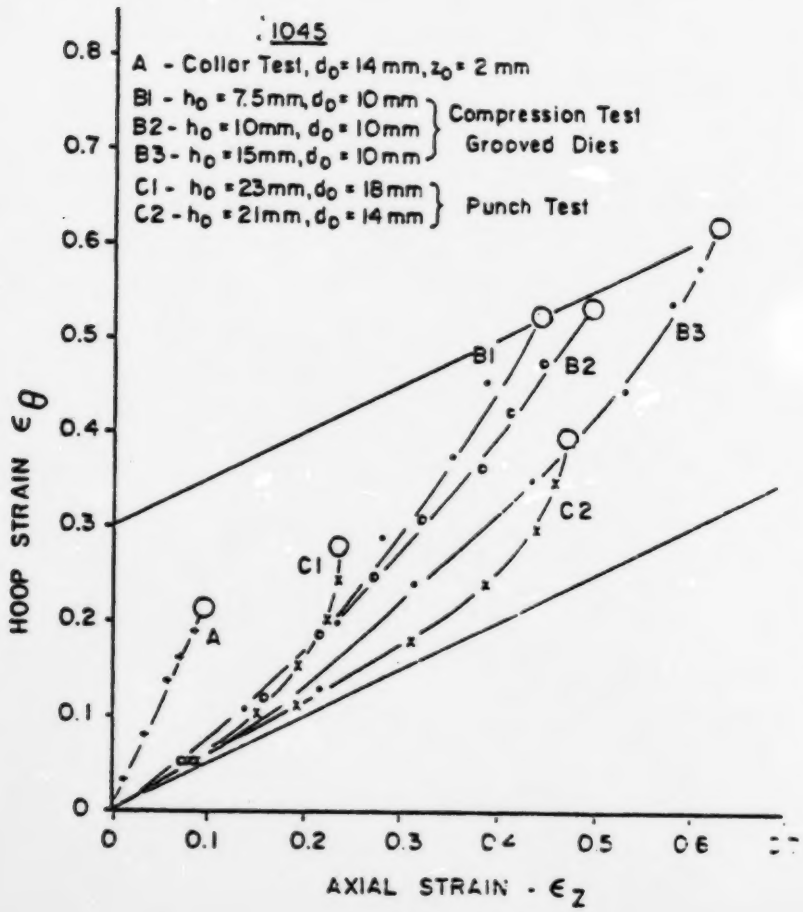

FIG. 2

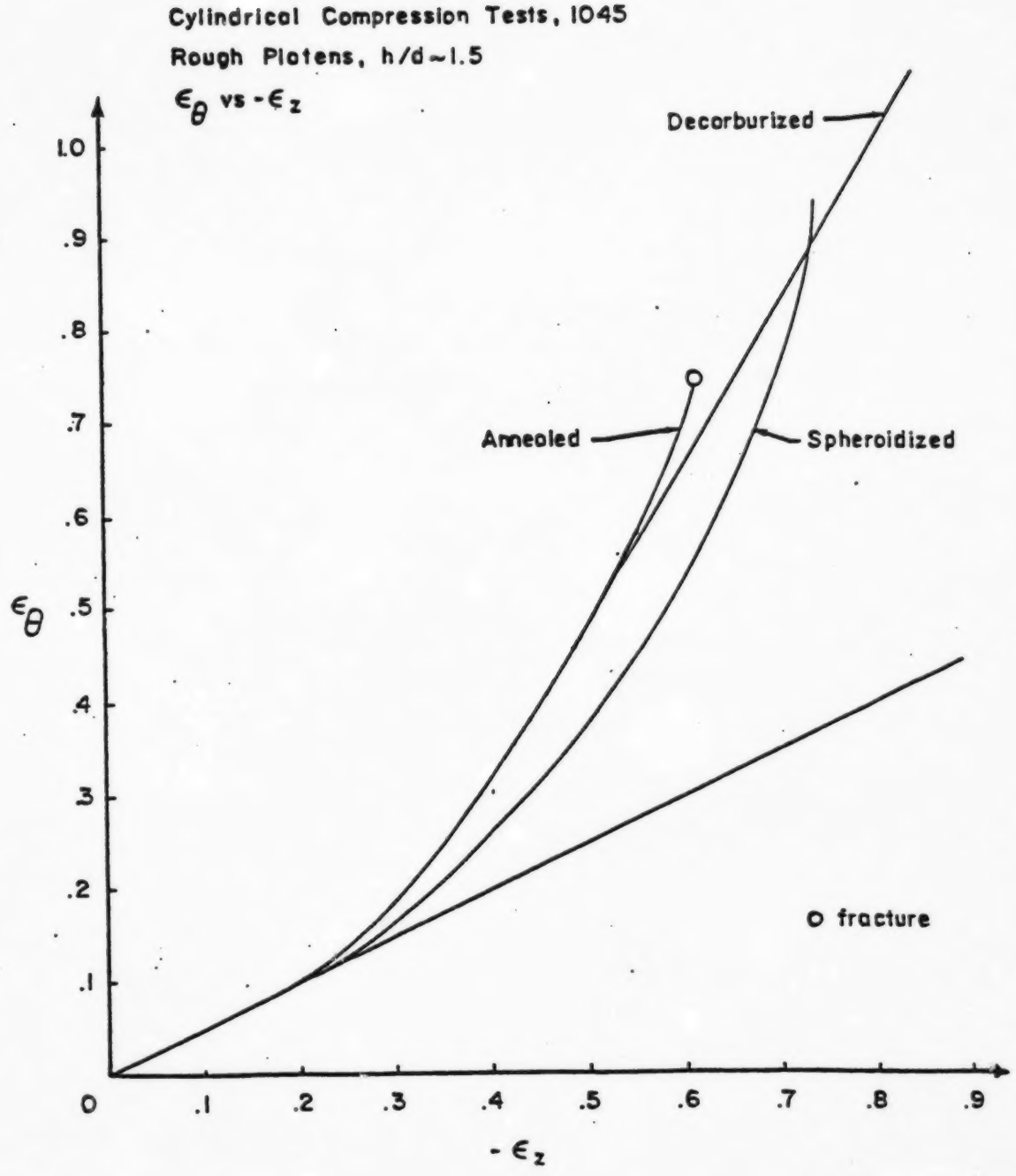
Cylindrical Compression Tests, 1045
Rough Platens, h/d ~ 1.5
ϵ_θ vs $-\epsilon_z$
Decorburized
Annealed
Spheroidized
O fracture
ϵ_θ
$-\epsilon_z$
0
.1
.2
.3
.4
.5
.6
.7
.8
.9
1.0

Fig. 3

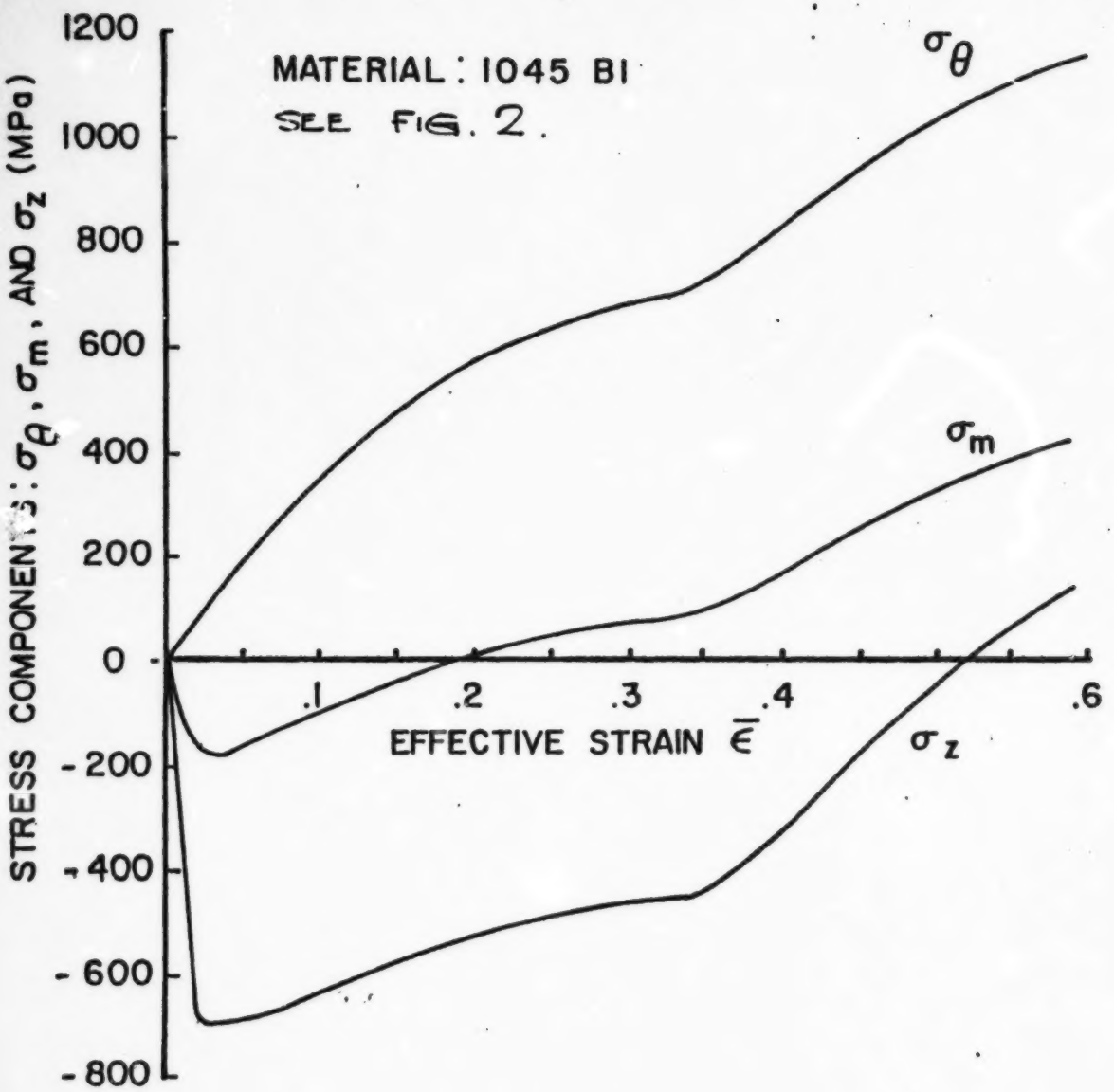
MATERIAL: 1045 BI
SEE FIG. 2.
STRESS COMPONENTS: σ_θ, σ_m, AND σ_z (MPa)
1200
1000
800
600
400
200
0
-200
-400
-600
-800
.1
.2
.3
.4
.6
EFFECTIVE STRAIN $\bar{\epsilon}$
σ_θ
σ_m
σ_z

FIG. 4

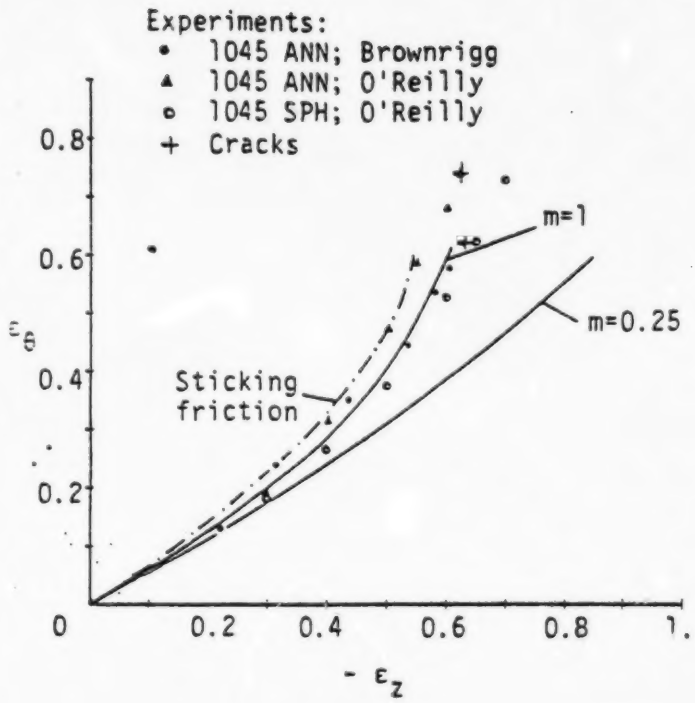

FIG. 5

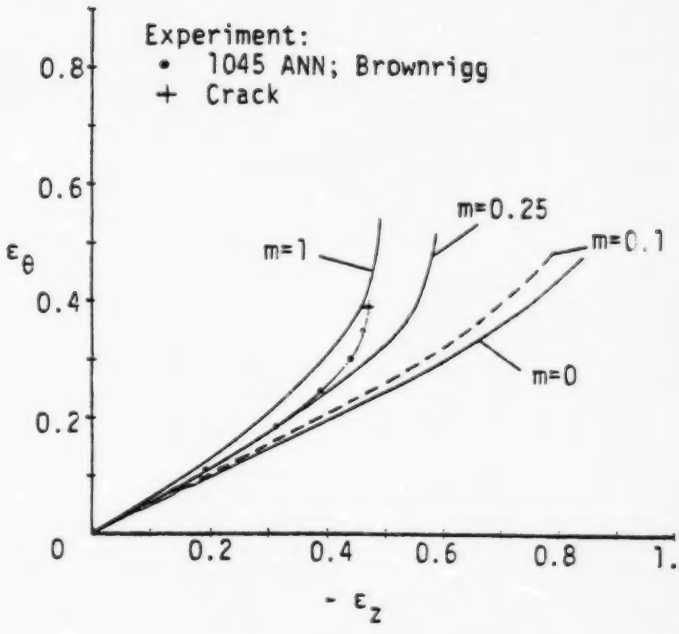

FIG. 6

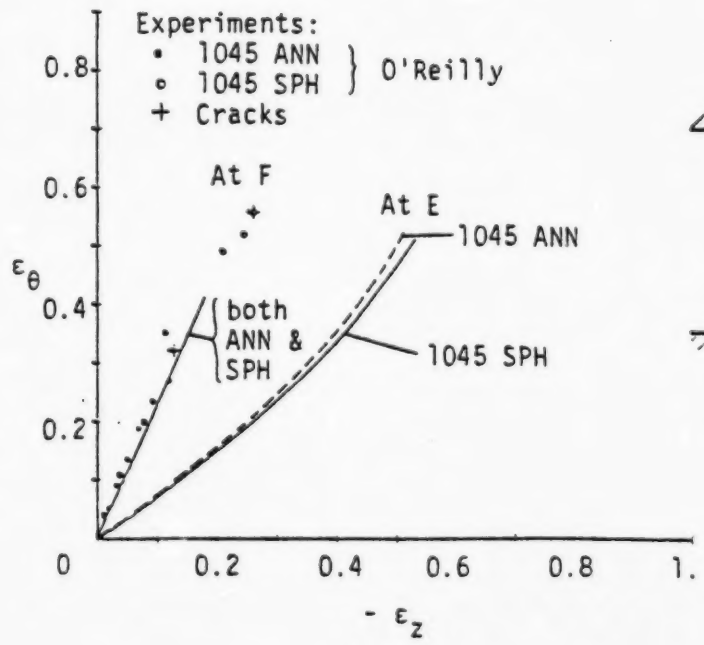

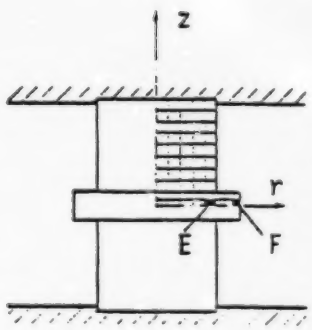

FIG. 7

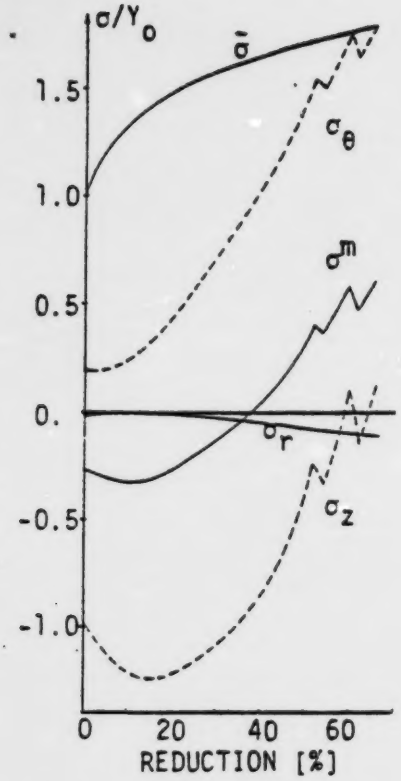

FIG. 8

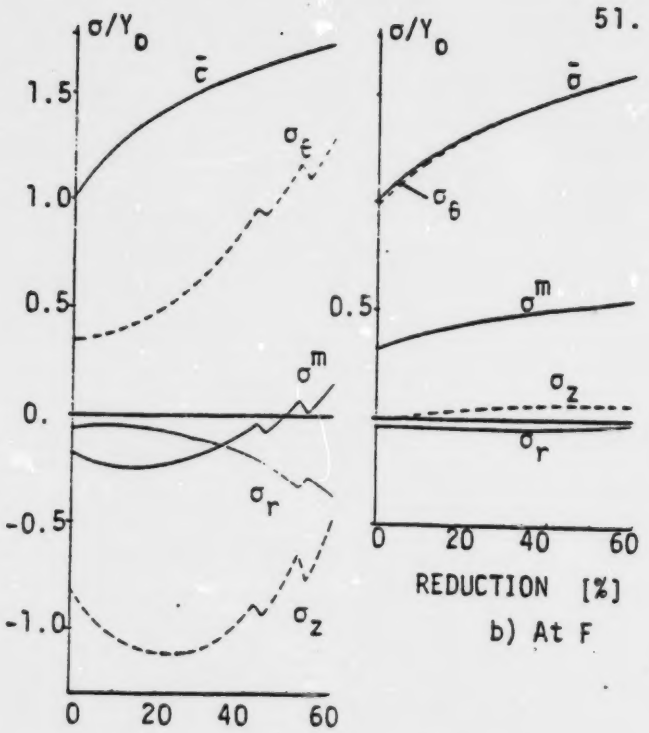

FIG. 9

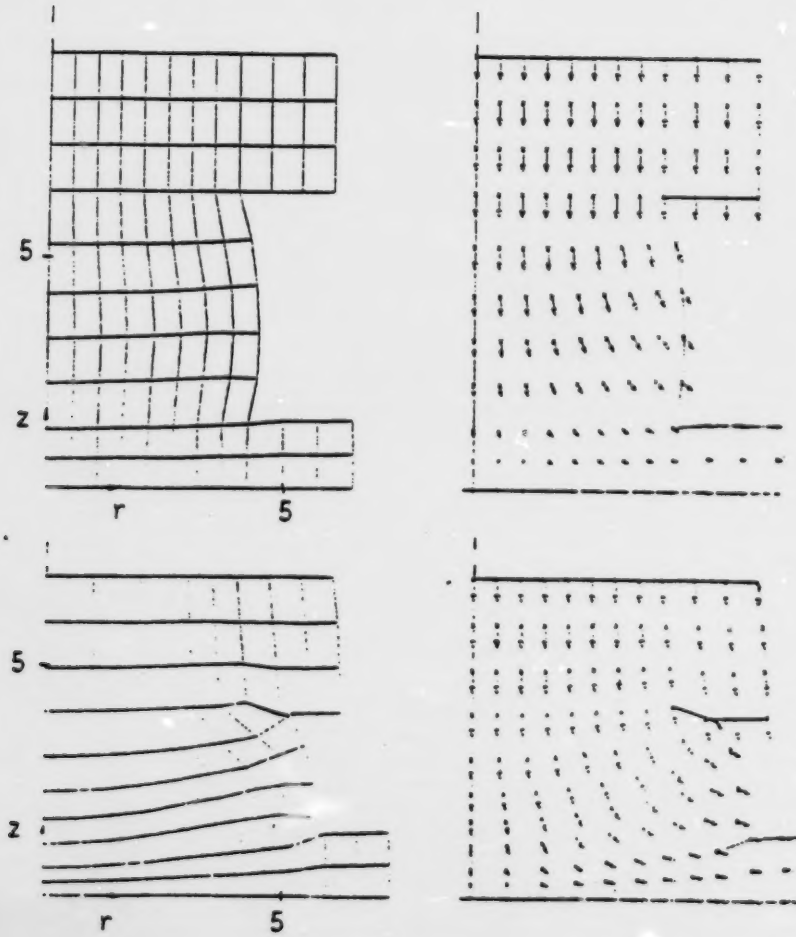

FIG. 10

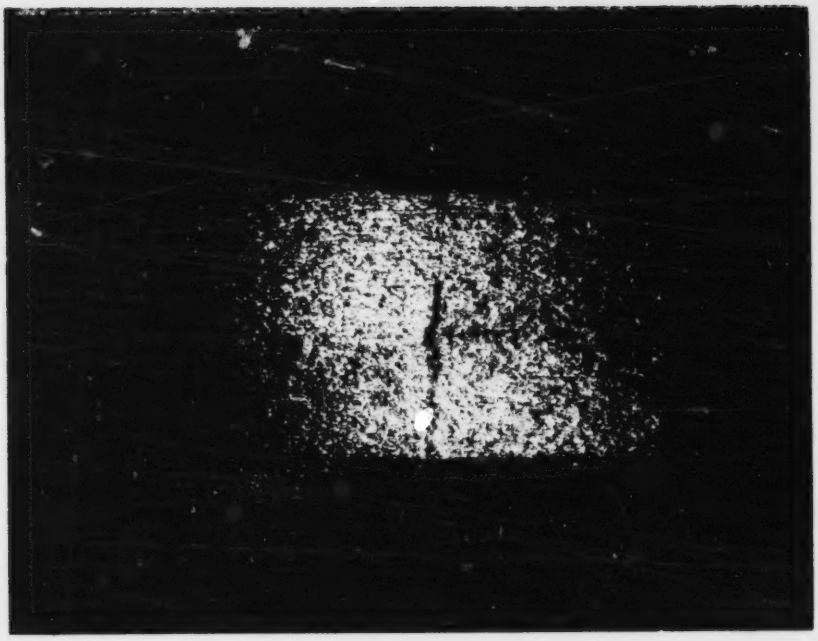

Fig. 11.a: Shear Crack on the Surface of a 1095 Cylindrical Sample, 6X.

Fig. 11.b: Void Sheeting on the Fracture Surface of the Above Sample, 1250X.

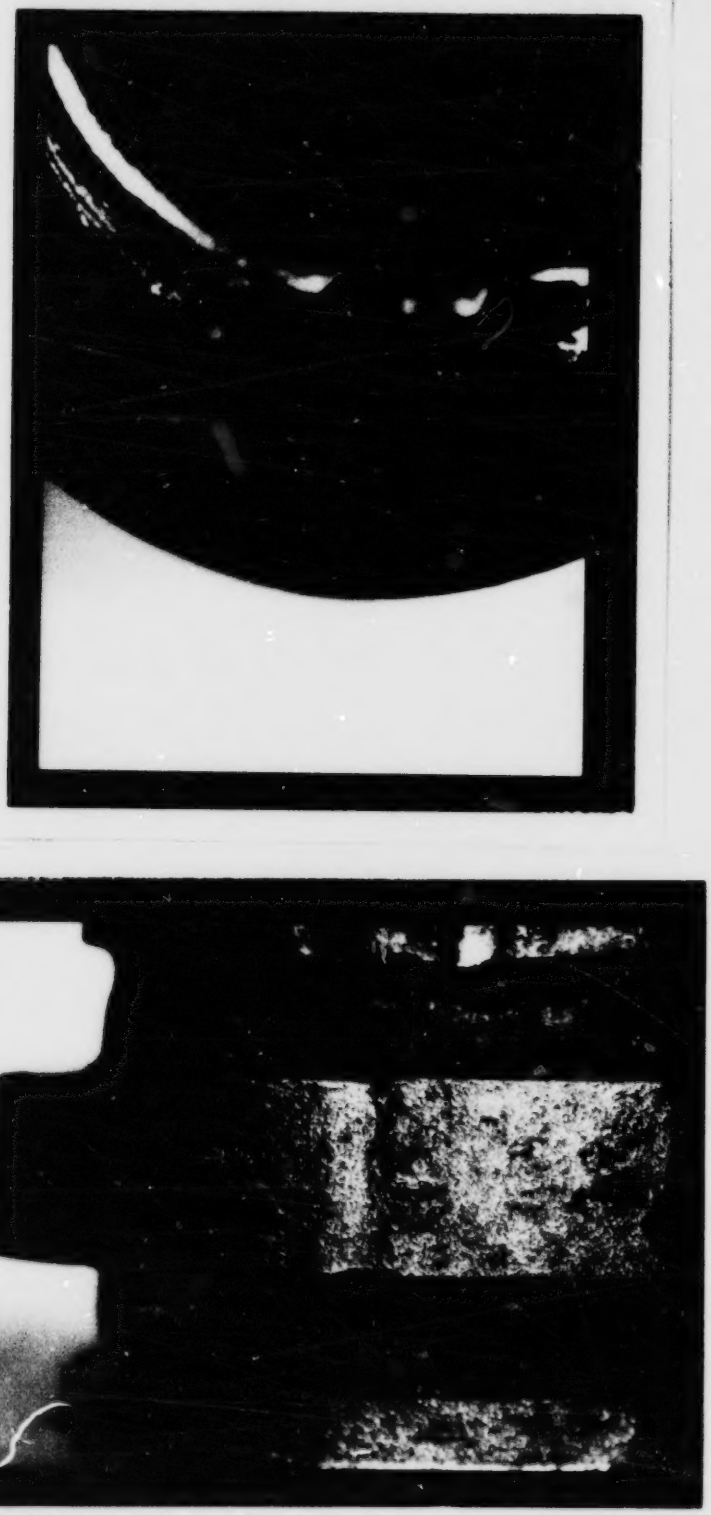

Fig. 12: Micrographs of Surface Instability in 1541 Collar Test, a) 7X, b) 10X

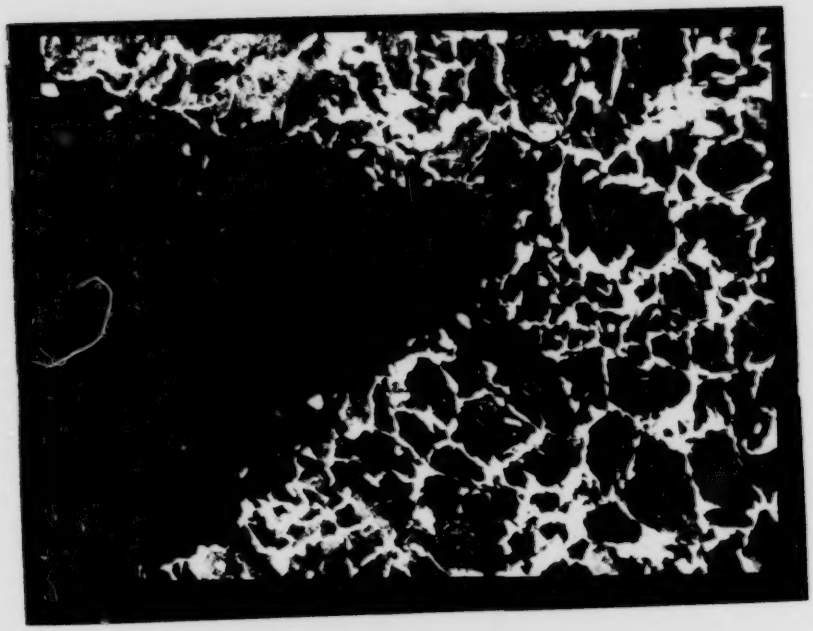

Fig. 13: Fracture Path in an 1144 Cylindrical Sample, 160X.

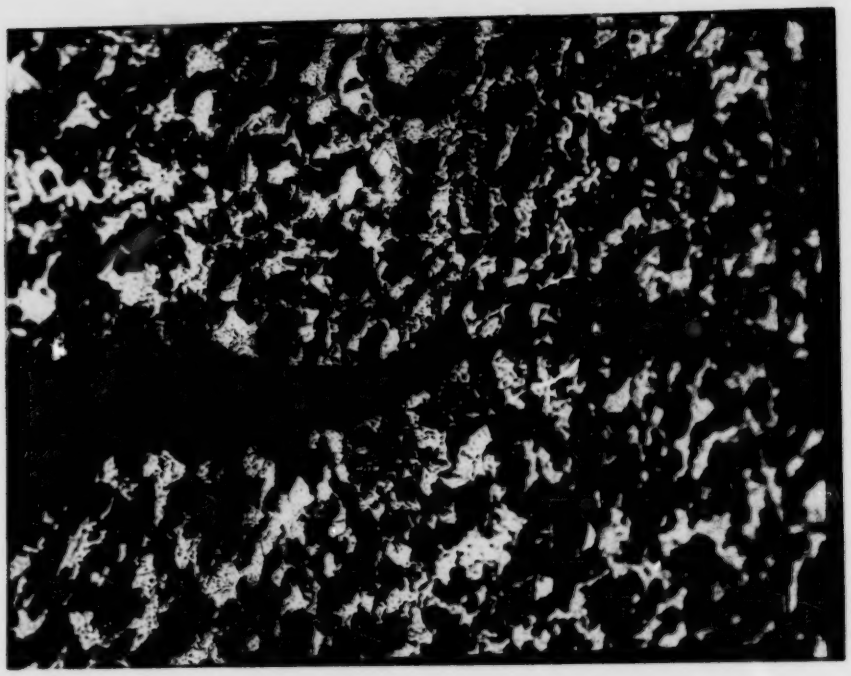

Fig. 14: Fracture Path in a 1045 Cylindrical Sample, 350X.

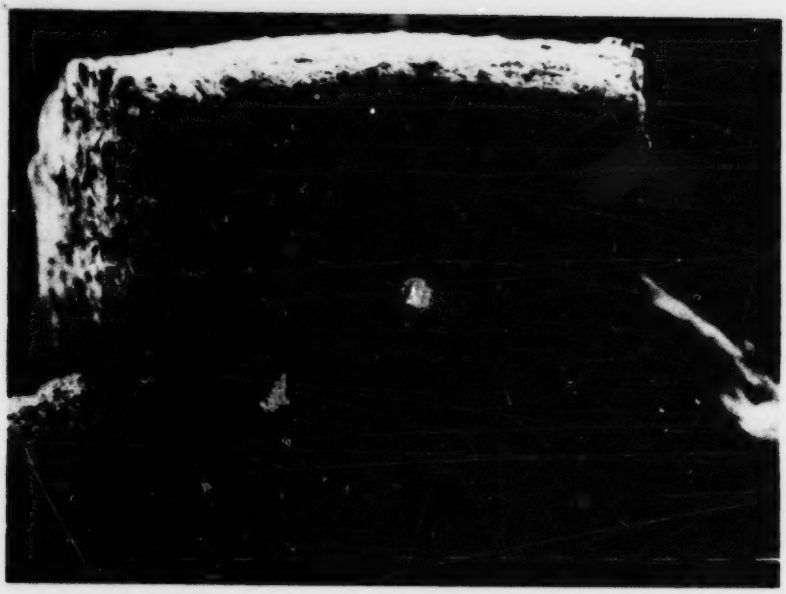

Fig. 15: Fracture Surface of a 1045 Spheroidized Collar Sample, Note the line associated with the surface instability, 40X.

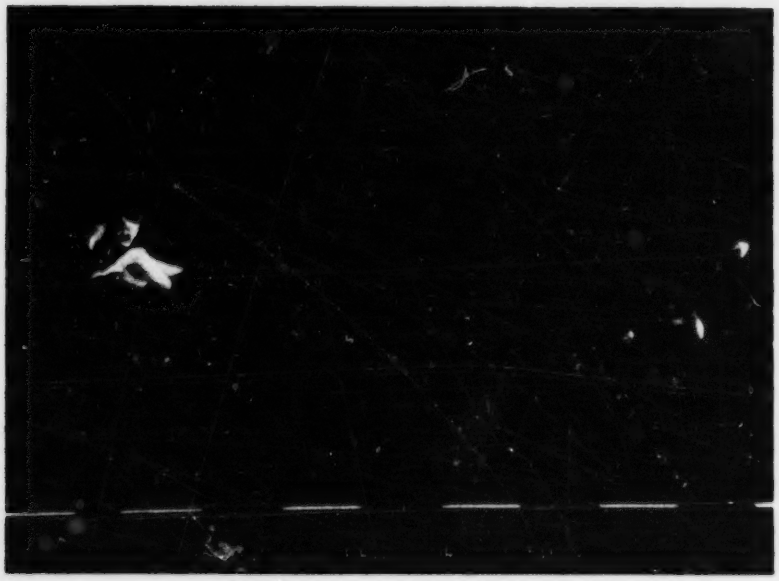

Fig. 16: S. E. M. Micrograph of an Aluminate Inclusion Stringer Associated with a Surface Instability in a 1045 Collar Sample, 2500X.

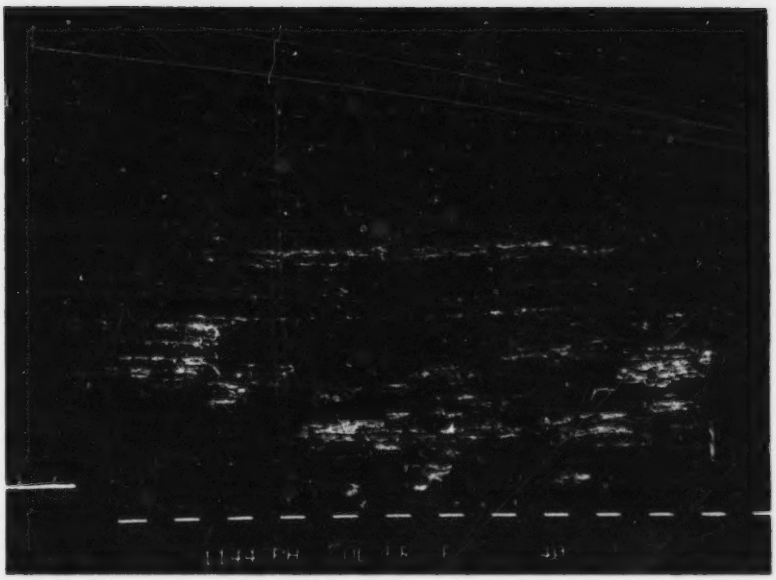

Fig. 17: Fracture Surface of a Spheroidized 1144 Collar Sample, 40X.

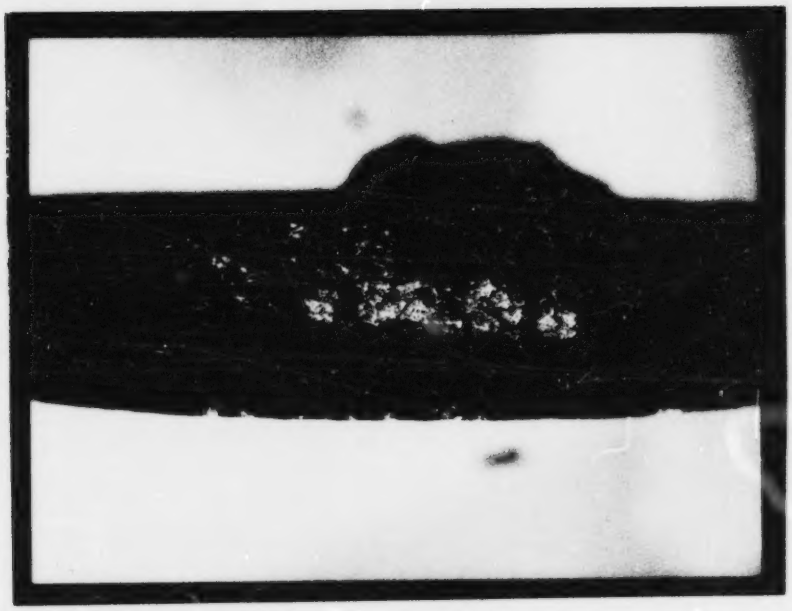

Fig. 18. Macrograph of intergranular cracks on the surface of a cylindrical Fe-1.2P sample, 6X.

COMPRESSION TEST $h_o / d_o = 1.5$

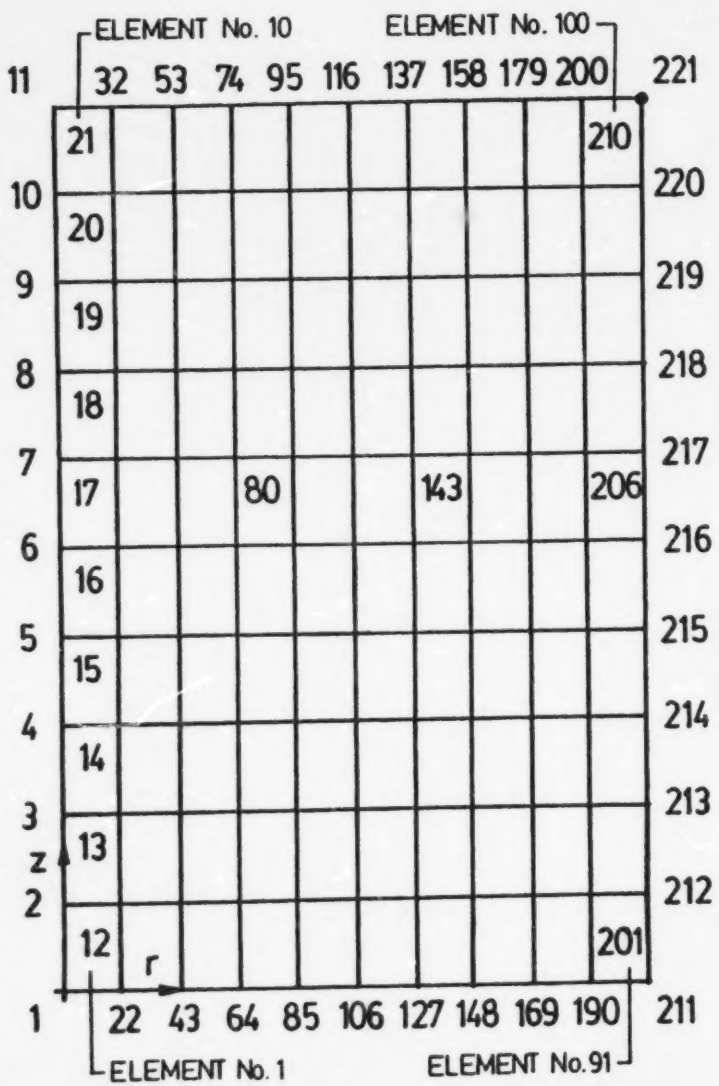

b) FINITE ELEMENT MESH
(100 ELEMENTS & 221 NODES)

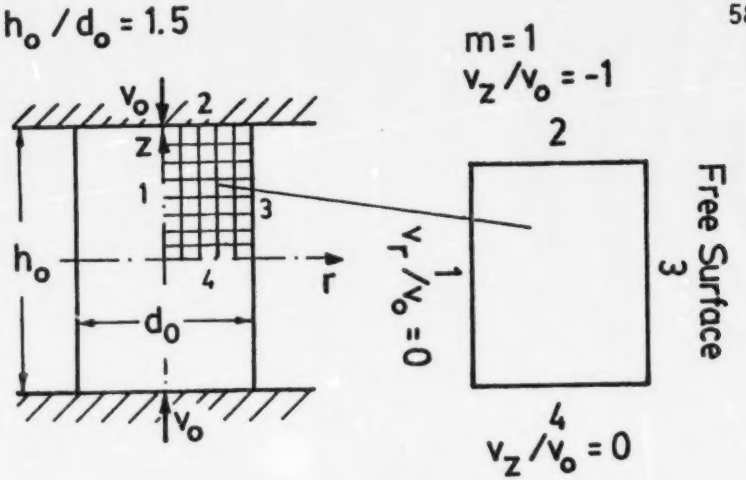

a) BOUNDARY CONDITIONS

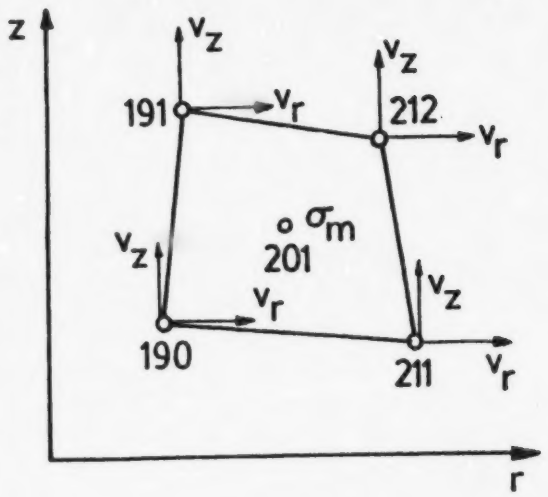

c) QUADRILATERAL ELEMENT No. 91

Fig. 19 Finite Element Model of the Compression Test.